SARS-CoV-2 promotes microglial synapse elimination in human brain organoids

Samudyata[1#], Ana Osório Oliveira[1#], Susmita Malwade[1], Nuno Rufino de Sousa[2], Sravan K Goparaju[1], Jessica Gracias Lekander[1], Funda Orhan[1], Laura Steponaviciute[2], Martin Schalling[3], Steven D Sheridan[4], Roy H. Perlis[4], Antonio Rothfuchs[2], Carl M. Sellgren[1,5]*

[1]Department of Physiology and Pharmacology, Karolinska Institute, Stockholm, Sweden.

[2]Department of Microbiology, Tumor and Cell Biology, Karolinska Institute, Stockholm, Sweden.

[3]Department of Molecular Medicine and Surgery, Karolinska Institutet and Center for Molecular Medicine, Karolinska University Hospital, Stockholm, Sweden.

[4]Center for Genomic Medicine and Department of Psychiatry, Massachusetts General Hospital, Boston, MA, USA.

[5]Centre for Psychiatry Research, Department of Clinical Neuroscience, Karolinska Institutet & Stockholm Health Care Services, Stockholm County Council, Karolinska University Hospital, Stockholm, Sweden.

[#] These authors contributed equally to this work

*To whom correspondence should be addressed: Carl M Sellgren, Dept. of Physiology and Pharmacology, Biomedicum C5, Solnavägen 9, 171 65 Solna, Sweden. Email: carl.sellgren@ki.se

ABSTRACT

Neuropsychiatric manifestations are common in both the acute and post-acute phase of SARS-CoV-2 infection, but the mechanisms of these effects are unknown. In a newly established brain organoid model with innately developing microglia, we demonstrate that SARS-CoV-2 infection causes an extensive cell death and loss of post-synaptic termini. Despite limited neurotropism and a decelerating viral replication, we observe a threefold increase in microglial engulfment of postsynaptic termini after SARS-CoV-2 exposure. We define the microglial responses to SARS-CoV-2 infection by single cell transcriptomic profiling and observe an upregulation of interferon-responsive genes as well as genes promoting migration and synaptic stripping. To a large extent, SARS-CoV-2 exposed microglia display a transcriptomic profile previously observed in neurodegenerative disorders characterized by early a synapse loss and an increased incident risk after a Covid-19 infection. Our results reveal that brain organoids infected with SARS-CoV-2 display disruption in circuit integrity via microglia-mediated synapse elimination and identifies a potential novel mechanism contributing to cognitive impairments in patients recovering from Covid-19.

34 **INTRODUCTION**

35 A significant proportion of patients infected with severe acute respiratory syndrome
36 coronavirus 2 (SARS-CoV-2), the causative agent of coronavirus disease 2019 (COVID-19),
37 display acute neurological and psychiatric symptoms[1]. Despite a low neural expression of the
38 major receptor (angiotensin-converting enzyme 2; ACE2) for SARS-CoV-2 entry, autopsy studies
39 have also detected the presence of SARS-CoV-2 RNA and protein in brain tissue of around half
40 of the examined COVID-19 patients[2]. Survivors then commonly report persistent central
41 nervous system (CNS)-related symptoms, such as memory loss and sleep disturbances[3], as well
42 as depressive symptoms[4]. In line with these findings, a subset of the patients also demonstrate
43 widespread disruptions to micro-structural and functional brain integrity in the recovery
44 stages[5]. Further, the risk of receiving a neurological or psychiatric diagnosis related to cognitive
45 impairment or behavioral abnormalities, including dementia, parkinsonism, or a psychotic
46 disorder, is increased also in non-hospitalized patients up to at least 6 months after infection, as
47 compared to other respiratory tract infections and with influenza[6,7,3]. Long-lasting
48 neurobehavioral and cognitive impairments are also common features of other RNA viruses
49 with a neuro-invasive potential, with the CNS-damaging processes also continuing after virus
50 elimination[8]. So far, the mechanisms causing neurocognitive sequelae after viral encephalitis
51 are poorly understood, but recent studies in rodents suggest that interferon-responses in
52 microglia can lead to excessive microglial synapse elimination and disruption of neuronal circuit
53 integrity[9,10].To some extent, this could explain why the developmental period of infection
54 influences the extent of neurocognitive sequelae[11] , as microglial functions involving circuit
55 refinement exhibit a clear temporal pattern during neurodevelopment[12].

56

57 Human brain organoids have been successfully employed to study neurotropism and neurotoxic
58 effects of viruses such as the Zika virus[12,13], and now more recently SARS-CoV-2[14–18]. However,
59 as microglia are of non-ectodermal origin[19,20], and the predominate germ layer fate in embryoid
60 bodies is ectodermal, brain organoids typically lack innately developing microglia. This has
61 limited the mechanistic understanding of microglial cellular responses in viral CNS infection,
62 such as in COVID-19, as well as understanding of cellular responses of astrocytes and neurons in
63 the context of surveying microglia.

64

65 In this study, we address this limitation by using a newly established protocol for generating
66 undirected brain organoids with innately developing microglia that arise from Brachychury^{+}
67 mesodermal progenitors[21]. Despite a low multiplicity of infection (MOI) resulting in a modest
68 infection, we observe an extensive neuronal cell death and a decrease in postsynaptic density
69 secondary to microglial synaptic stripping. We perform single cell RNA sequencing (scRNA-seq)
70 to characterize the temporal dynamics of single cell responses in infected organoids, and
71 observe a cluster of interferon responsive microglia, also defined by an upregulation of genes
72 promoting migration and microglial synapse elimination, that largely overlap with the
73 transcriptomic profile observed in neurodegenerative disorders characterized by an early
74 synapse loss and an increased incident risk after a Covid-19 infection. These results indicate
75 that SARS-CoV-2 has the potential to disrupt neuronal circuit integrity via microglia-mediated
76 synapse elimination and identifies a potential novel mechanism contributing to cognitive
77 impairments in patients recovering from Covid-19.

78

79 **RESULTS**

80 *Limited neurotropism but extensive cell death and synapse loss in infected brain organoids*

81 With a few modifications (see **Methods** and **Fig. 1a**), the protocol reported by Ormel et al.[21]
82 was adapted to miniaturized bioreactors and used to generate undirected brain organoids.
83 After 56 days in vitro (DIV), these undirected organoids were found to contain neural
84 progenitor cells (NPCs; PAX6$^+$), neurons (β-tubulin$^+$ and MAP2$^+$), neural crest cells (SOX10$^+$),
85 cells of astrocytic lineage (GFAP$^+$ and S100B$^+$ at 56 DIV and AQP4$^+$ at 110 DIV; **Supplementary**
86 **Fig. 1a**), along with microglia (IBA1$^+$ and CD68$^+$); **Fig. 1b**. We exposed such organoids to active
87 SARS-CoV-2 virus for 2h at an estimated MOI of 0.3, after which they were washed and
88 transferred into fresh media to monitor the course of infection. Supernatants were harvested
89 at 6, 24, 48, 72 hours post-infection (hpi) for viral replication assessment. Viral RNA-dependent
90 RNA polymerase (*Rdrp*) and nucleocapsid (*N*) transcription were measured in supernatants via
91 RT-qPCR and we observed a time dependent increase for both these transcripts (**Fig. 2a** and
92 **Supplementary Fig. 1b**), indicating the virus is capable of initiating RNA replication of its
93 genomic material within the cells of the organoid, but at a slower pace as compared to Vero-E6
94 cells (**Supplementary Fig. 1b**). To validate SARS-CoV-2 could assemble and release complete
95 viral particles in the organoids, we performed plaque formation assays using supernatants from
96 infected organoids and observed an release of infectious viral particles as early as 6hpi,
97 although the number of plaque forming units (PFUs) then quickly decreased (**Fig. 2b**).

98

99 At two time points (24 and 72hpi), we fixed infected and uninfected organoids (56 DIV) for
100 immunohistochemical (IHC) analyses. At 24hpi, a strong signal for the viral nucleocapsid protein
101 (NP) was observed mainly in the periphery of the infected organoids, whereas at 72hpi, we
102 observed NP staining in cellular cytoplasm or processes of infected cells (**Fig. 2c**). On average,
103 around 3% of the cells in the superficial layers of the organoids were found to be NP^+ at 72hpi
104 (**Supplementary Fig. 1c**). Cleaved caspase3 (CASP3) staining revealed extensive cell death in the
105 infected organoids as compared to the uninfected organoids, occurring already at 24hpi (**Fig.**
106 **2d**). $Casp3^+$ cells were not just limited to superficial layers like NP^+ cells and the number of
107 $Casp3^+$ cells greatly exceeded the number of NP^+ cells at both timepoints (**Supplementary Fig.**
108 **1c**). Infected organoids also displayed a clear decrease in postsynaptic density as compared to
109 control organoids, and at 72hpi, organoids displayed a 50% decrease in post-synaptic density as
110 measured by PSD-95 (**Fig. 2e**).
111
112 Next, we investigated infectivity and cell death in the context of cellular identity. IHC staining
113 on infected organoids at 72hpi showed viral NP overlapping with $PAX6^+$, $MAP2^+$, $GFAP^+$, ,
114 $SOX10^+$, and $OLIG2^+$ cells; **Fig. 3a-f**). $CASP^+$ staining was foremost observed in neurons, but also
115 included other cell types (**Supplementary Fig. 1e).** In addition, we detected $IBA1^+$ cells that
116 stained positive for dsRNA (**Fig. 3f**) although the scarcity of these cells (slightly below 1% on
117 average) obstructed meaningful quantifications. Therefore, we enriched for microglia from two
118 infected organoids using magnetic-activated cell sorting (MACS) with CD11b beads. qRT-PCR on
119 cell lysates suggested the capture of fetal microglia (*AIF1* expression, no *TMEM119*
120 expression[22]; **Supplementary Fig. 1f**) including viral *N* gene copies (**Fig. 3g**). Further, we derived

121 induced human microglia-like cells (iMGs) in 2D-culture[23], and exposed these cells to live SARS-
122 CoV-2 virus (MOI=0.01). At 24hpi, we detected dsRNA^{+} cells (**Supplementary Fig. 1g**), indicating
123 the presence of virus inside iMGs.
124
125 *Increased microglial stripping of postsynaptic termini in infected organoids*
126 Previous studies using murine models have shown that neuroinvasive RNA viruses can cause
127 microglial engulfment of synaptic termini[9,10]. To determine if SARS-CoV-2 also has the capability
128 to induce synaptic stripping and contribute to the observed decrease in postsynaptic density
129 observed in infected organoids, we first investigated to what extent microglia contributed to
130 synapse remodeling in uninfected organoids (110 DIV). In line with our previous findings in 2D
131 models[24], super-resolution imaging revealed a baseline uptake of postsynaptic structures
132 (indicated by PSD-95) in microglia residing in brain organoids (**Fig. 4a-c**). In infected organoids
133 (72hpi), this uptake was increased by threefold (**Fig. 4d**), indicating that SARS-CoV-2 infection
134 can perturb the integrity of neuronal circuits by promoting excessive microglial synapse
135 engulfment. Notably, the observed synapse loss (as well as neuronal apoptosis) greatly
136 exceeded neuronal infectivity.
137
138 *Single cell characterization of brain organoids containing resident immune cells*
139 Droplet-based encapsulation of single cells using the 10X Genomics chromium system allowed
140 us to profile and compare transcriptomes of individual cells isolated from SARS-CoV-2 infected
141 brain organoids as compared to uninfected control organoids. Given the extent of cell death in
142 the organoids exposed to an estimated MOI of 0.3, we then decreased the MOI to 0.1. Since

143 microglial numbers were low in 56 DIV organoids, we also used organoids cultured up to 110
144 DIV and enriched for CD11b^{+} cells (MACS). In this way we were able to obtain good-quality
145 transcriptomic data from fresh cells isolated in three experimental conditions: uninfected
146 control organoids (7257 cells), 24hpi organoids (15254 cells), and 72hpi organoids (2825 cells),
147 respectively (**Supplementary Fig. 2b)**. Then, we integrated pre-processed data from each
148 condition and performed unsupervised graph-based clustering to obtain cellular clusters with
149 similar transcriptomic identities across conditions (**Fig. 5a**, **Supplementary Fig. 2a-d)**.
150 Supervised inspection of top differentially expressed genes (DEGs) per cluster combined with
151 cell type-specific gene signatures and cluster correlations to other developing human brain[25–
152 31], as well as organoid[32–34], datasets confirmed 16 clusters (**Fig. 5b-d**, **Supplementary table 1,**
153 **Supplementary Fig. 3, 4a-e**). To address if organoid grown microglia at 110 DIV resembled adult
154 or fetal primary microglia, we performed integration of single cell RNA sequencing data
155 from our microglia cluster with two primary fetal microglia dataset[25,29], as well as a primary
156 adult dataset[30], and concluded that the overall transcriptomic profile was closest to fetal
157 microglia (**Supplementary Fig. 4f**).
158
159 *Confirming the expression of SARS-CoV-2 entry factors*
160 We then assessed the expression of previously identified entry factors for SARS-CoV-2 in the
161 generated single cell data and observed that the overall basal RNA expression was relatively
162 low (**Fig. 6a**). However, to some extent, we may have at least partly underestimated *ACE2*
163 expression by enriching for viable cells displaying low tropism and low *ACE2* expression, or not
164 thoroughly capturing *ACE2* expression at the present sequencing depth. In line with previous

165 reports, cells belonging to the choroid plexus showed relatively higher *ACE2* expression[18,35], and
166 we also observed a more pronounced expression in a subset of neurons with midbrain
167 dopaminergic markers (**Fig. 6a, Supplementary Fig. 4g).** However, this subset of neurons did
168 not exhibit any differential response in relation to other neuronal clusters across conditions
169 (**Supplementary table 3**). Consistent with an underestimation of *ACE2* expression due to e.g.,
170 negative selection based on viability, we observed more robust and heterogenous neuronal
171 ACE2 staining using IHC (**Supplementary Fig. 4h**). Similar to *ACE2* expression, proteases
172 involved in viral S protein priming [39] (*TMPRSS2* and *TMPRSS4*) also displayed low expression,
173 whereas *FURIN* [36] and infection potentiating factor (Neuropilin 1: *NRP1*,) had a wider cell type
174 distribution which included astrocytes, perivascular cells, endothelial cells and microglia (**Fig.**
175 **6a**). Microglia also expressed other predicted entry factors (*CTSL* and *CTSB,* Cathepsin L and B*)*,
176 purported to act as substitutes for TMPRSS2 [37] (**Fig. 6a**). Next, we identified infected cells by
177 aligning cellular viral transcripts to the whole SARS-CoV-2 genome in the infected conditions.
178 The percentage of infected cells was low (0.1-0.2% of sequenced cells), which was expected
179 given the lower MOI and to some extent removal of non-viable infected cells, although we were
180 able to qualitatively identify infected neurons, radial glia, astrocytes, and choroid plexus cell
181 types (**Supplementary table 2**). Amongst the infected cells, we observed a preferential infection
182 of neurons (p=0.009) and radial glia (p=0.027). For further downstream analyses, we did not
183 make any distinction between infected and non-infected cells, instead focusing on overall
184 cellular responses in the infected conditions.
185
186

187

188 *Interferon responsive microglia with upregulation of genes promoting synapse elimination*

189 To define microglial responses to SARS-CoV-2 exposure, we first performed pseudo-bulk
190 differential gene expression testing across the three experimental conditions, i.e., uninfected
191 control organoids, and organoids 24hpi and 72hpi. An unbiased hierarchical clustering approach
192 generated two unique groups of DEGs (labeled module A and B). Module A comprised of genes
193 whose expression on average decreased at 24hpi and then at 72hpi displayed a more
194 pronounced increase, while module B genes on average displayed reduced expression at 24hpi
195 and a more dramatic decrease at 72hpi (**Fig. 6b**). While module B was largely comprised of
196 genes encoding for cytosolic ribosomal proteins (**Supplementary Fig. 5e**), we detected several
197 interferon-stimulated genes (ISGs) in module A such as *ISG15*, *MX1*, *MX2*, *RSAD2* and *BST2* (**Fig.**
198 **6c, Supplementary table 4**). Accordingly, IHC validation of ISG15 protein expression showed a
199 general increase in interferon response in organoids at 72hpi as well as a specific upregulation
200 in IBA1^{+} cells, compared to control organoids (**Fig. 6d, Supplementary Fig. 5j**). Nonetheless, we
201 detected no clear upregulation of pro-inflammatory cytokines in microglia, at either 24hpi or at
202 72hpi, although several pathogen sensors and upstream effectors of interferon signaling were
203 upregulated including nuclear factor kappa B (*NFKB1*) (**Fig. 6e**). At 24hpi, we detected
204 upregulation of pathways (such as oxidative phosphorylation, release of calcium into cytosol,
205 monovalent inorganic ion transport, lysosomal disruption and hypoxia; **Supplementary Table 3**)
206 that can serve as activating stimuli for primed inflammasome components (*NLRP3*, *PYCARD*,
207 *CASP1*), and are required for the production and maturation of pro-inflammatory cytokines (**Fig.**

208 **6e)**[38]. Taken together, this suggests that SARS-CoV-2 activates interferon signaling in microglia
209 although the expression of pro-inflammatory cytokines are at normal levels already at 24hpi.
210
211 In the infected conditions, we in unbiased analyses observed a significant upregulation of
212 pathways related to neurodegenerative diseases, including Alzheimer's disease (AD) and
213 Parkinson disease (PD) (**Supplementary Fig. 5f**). Notably, both these disorders are characterized
214 by a microglia-mediated early synapse loss[39], and display an increased incident risk after Covid-
215 19 infection[3]. This led us to examine the microglial transcriptional state more closely after
216 exposure to SARS-CoV-2 in relation to previously described disease-associated microglial
217 activation states. First, we compared SARS-CoV-2-exposed microglia to such activation states
218 observed in experimental murine models. Injury responsive microglia (IRM) have been
219 described in mice close to experimentally induced focal demyelination (7 days post lesion) and
220 are to a large extent defined by upregulation of ISGs[40,41], while the disease-associated microglia
221 (DAM) described in mouse models of AD and ALS are thought to restrict neurodegeneration
222 and disease development[42]. SARS-CoV-2 exposed microglia then displayed a significant
223 enrichment for genes associated with the IRM activation state ($p=6.9x10^{-24}$, **Fig. 6f**), and less so
224 for the unique DAM signature genes (p=0.11), while still displaying upregulation of genes
225 implicated in AD such as *APOE*, *CTSZ* and *GRN* with a non-significant decrease of core microglial
226 homeostasis genes (*P2RY12*, *CX3CR1*, *P2RY13*, *CD33*, *TXNIP*; **Supplementary Fig. 5g-h).** In fact,
227 *APOE* and *CTSZ* were observed to be commonly dysregulated across all three signatures (IRM,
228 DAM and SARS-CoV-2 exposed microglia), suggesting unique as well as shared activation
229 mechanisms across these microglial states. Further, we compared the SARS-CoV-2 microglial

230 transcriptomic signature to previously identified human microglial populations identified in
231 autopsy and surgical brain tissues obtained from subjects in the Memory and Aging Project
232 (MAP)[43], and found an enrichment with genes in so-called interferon responsive microglia
233 (cluster 4 in this dataset) (**Fig. 6g**), defined by *ISG15* and with increased expression of multiple
234 sclerosis (MS) and AD susceptibility genes. To exclude effects of tissue processing, we also
235 compared microglia from the organoids with a cluster defined by general cellular distress due
236 to tissue processing (cluster 3) but observed no enrichment (**Fig. 6g**).
237
238 Actin-cytoskeletal remodeling pathways, essential for promoting migration and phagocytosis,[44]
239 were also upregulated in microglia exposed to SARS-CoV-2 **(Fig. 6h, Supplementary Fig. 5f).**
240 Consistent with this upregulation in microglia, and the extensive neuronal cell death and
241 decreased postsynaptic density in infected organoids, neurons at 72hpi downregulated the
242 expression of 'don't-eat-me' signals such as *CD46* and *CD200* (**Supplementary Fig. 5i**)[45].
243 Consequently, we observed increased microglial expression of genes associated with microglia-
244 mediated phagocytosis[46–49], such as *CD68*, *TREM2*, *ITGB5*, *CD47, MSR1, CALR*, as well as genes
245 previously identified to be directly involved in synapse elimination in the aftermath of viral
246 encephalitis, such as *C3*, *C3AR1* and *FCGR3A*[8] (**Supplementary Fig. 5h)**.
247
248 In summary, this suggests that microglia in response to SARS-CoV-2 exposure quickly adopt
249 transcriptional states that are unique but also overlap with signals observed in
250 neurodegenerative diseases, and that these states are likely to include both protective — e.g.,

251 clearing of debris and defense, as well as detrimental — e.g., inducing excessive neuronal
252 apoptosis, and synaptic stripping responses.
253
254 *Astrocytic subclusters with enrichment for genes implicated in neurodegenerative diseases*
255 In response to SARS-CoV-2, astrocytes displayed DEGs enriched for mechanisms involved in cell
256 cycle, carbon metabolism and disorders such as Huntington's disease (HD) and PD (**Fig. 7a**).
257 Already at 24hpi, three subclusters of astrocytes could be identified: AS-0, AS-3 and AS-4 (**Fig.**
258 **7b**). AS-0 cells expressed relatively higher levels of anti-viral ISGs such as *IFIT1*, *ISG15*, and
259 *SCRG1*, while AS-3 and AS-4 cells had a proliferative profile (*TOP2A*, *MKI67*) and exhibited lower
260 expression levels of *GFAP* (**Fig. 7b-d**). Subcluster AS-2, comprising of cells sampled at 72hpi,
261 showed elevated levels of *GFAP* and *STAT3*, indicative of reactive astrogliosis[50], along with
262 phagocytosis related genes such as *MEGF8* and *ABCA1* (**Fig. 7c**). We also observed upregulation
263 of metal ion (zinc, copper, iron) homeostasis pathways involving metallotheionins (*MT2A*,
264 *MT1X*, *MT1E*) in AS-2 astrocytes at 72hpi (**Fig. 7d**).
265
266 In neurodegenerative diseases, astrocytes have been shown to express markers of a putative
267 reactive neurotoxic state commonly referred to as A1[51]. Given that astrocytic DEGs from
268 infected organoids were enriched for such diseases, we integrated single-cell transcriptomic
269 data from A1 astrocytes (stimulated with IL-1A, TNF-α and C1q)[52], and SARS-CoV-2 exposed
270 astrocytes via canonical correlation analysis (CCA). Although the majority of SARS-CoV-2
271 exposed astrocytes (AS-0, AS-1, AS-2) clustered separately from A1 astrocytes, the proliferative
272 clusters (AS-3 and AS-4), as well as a subset of AS-0 astrocytes, showed clustering similarities

273 with a portion of A1 astrocytes (**Fig. 7c**). Furthermore, higher expression levels of
274 metallotheionins, as in AS-2 cluster (72hpi), have been observed in astrocytes from HD
275 patients[53]. In summary, similar to the observed effects in microglia, we observe responses in
276 astrocytes to SARS-CoV-2 exposure that share features with detrimental cellular states
277 observed in neurodegenerative diseases, but also a strong temporal heterogeneity that
278 includes unique cellular states.
279
280 *Secretome alterations indicating a compromised capacity to keep BBB integrity*
281 Potential entry routes to the CNS for SARS-CoV-2 includes the blood-brain barrier (BBB) or the
282 blood-cerebrospinal-fluid-barrier (BCSFB), involve cell types such as endothelial cells, pericytes,
283 astrocytes and choroid plexus-epithelium. Upon encountering pathogens, these barrier cells act
284 in concert to activate and regulate signal transduction pathways that aid invasion of peripheral
285 immune cells and restoring of CNS homeostasis[54]. Correspondingly, at 24hpi we found
286 increased ligand-receptor communication between astrocytes, neurons, microglia, perivascular,
287 and endothelial cells**,** whereas at 72hpi, both microglia and neurons significantly reduced their
288 communication with most other cell types, while choroid plexus cell types gained interactions
289 (**Fig. 7g)**. Sub-clustering of choroid plexus related cells (**Fig. 7h**) showed two control enriched
290 clusters (CP-0 and CP-2), consisting of genes involved in maintaining solute homeostasis (*AQP1*),
291 barrier or extracellular matrix (ECM) integrity (*TIMP1*, *LGALS1*, *COL1A2*, *COL2A1*, *COL3A1*) and
292 amyloid clearance (*TTR*, *MT3*), amongst others (**Supplementary Fig. 7c**). At 24hpi, we observed
293 an enrichment of metallotheionins (*MT1M*, *MT1E*, *MT1X*, *MT1F*, *MT2A*: CP-6), similar to what
294 we observed in astrocytes at 72hpi, whereas genes involved in viral defense response

295 (*SAMHD1*), regulation of reactive oxygen species (ROS) (*SOD3*) and ECM organization (*FBLN1*,
296 *SYNE1*) were enriched at 72hpi (CP-5) (**Supplementary Fig. 7c**). In addition to choroid plexus,
297 differential expression analysis showed significant increase in expression of matrix
298 metalloproteases and ECM-regulatory enzymes (*MMP14*, *MMP9, LOX)* at 72hpi in microglia,
299 astrocytes and perivascular cells, whereas endothelial cells reduced expression levels of solute
300 carrier *SLC2A1* **(Fig. 7e)**, all in agreement with signaling that promotes compromised CNS
301 barriers. Accordingly, by IHC we further validated increased MMP14 protein expression by
302 PDGFRB$^+$ (pericytes) as well as GFAP$^+$ cells within 72hpi organoids (**Fig 7f-i**). Further, astrocytes,
303 pericytes and choroid plexus related cells were observed to downregulate VEGF signaling, a
304 potent inducer of BBB permeability, at 24hpi but then at 72hpi instead display an upregulation,
305 coinciding with increased signaling for leukocyte chemotaxis and activation in astrocytes, as
306 well as antigen processing and presentation in choroid plexus (**Fig. 7e**). In aggregate, this
307 suggest that cell types implicated in barrier functions change their communication upon SARS-
308 CoV-2 infection, indicative of compromised integrity, as well as altered secretome and signaling
309 with peripheral immune cells.
310
311 *Metabolic dysregulation across cell types*
312 Protein accumulation in the endoplasmic reticulum (ER) following viral infection or excessive
313 production of secretory proteins can induce ER stress and initiate counter measures in the form
314 of reduced translation and export to ER along with unfolded protein responses (UPRs).[55] In
315 exposed organoids, we detected an upregulation of pathways related to UPRs (IRE1, PERK), ER
316 stress, proteasomal degradation and autophagy, among cell types such as microglia, astrocytes,

317 choroid plexus and perivascular cells (**Supplementary Table 3**). Further, a partial translational
318 inhibition could be observed in microglia (module B, as discussed before), as well as most of the
319 other cell types (**Supplementary Table 3**, **Fig. 5h)**. We also observed a downregulation of the
320 ROS metabolism across cell types, which can lead to dysregulation of the antioxidant cellular
321 systems and result in oxidative stress[56]. SARS-CoV-2 then relies on excessive glucose for its
322 replication,[57] and shunts glucose from glycolytic pathways to fuel oxidative phosphorylation
323 and ATP production in a process known as the Warburg effect[58]. In our dataset, pathways
324 pertaining to cellular respiration (oxidative phosphorylation, electron transport chain coupled
325 to ATP synthesis) were enriched at 24hpi in neurons, while those of glucose and pyruvate
326 metabolism were downregulated (**Supplementary Table 3**). Furthermore, transcription of
327 glucose transporter, GLUT1 (*SLC2A1*), lactate dehydrogenase (*LDHA*) along with
328 monocarboxylate transporter, MCT4 (*SLC16A3*), was downregulated in astrocytes at 24 and
329 72hpi, indicating deficits in glucose export and redox cycling necessary for neuronal
330 energization[59] (**Supplementary Table 3**). This suggests that following exposure to SARS-CoV-2,
331 CNS cell types undergo major stress that results in metabolic changes which are likely to impact
332 cellular communication such as the important interplay between astrocytes and neurons.
333

334 **DISCUSSION**

335 Long-lasting neurobehavioral and cognitive impairments have been increasingly recognized in
336 the ongoing Covid-19 pandemic[6,7,60]. In the following 6 months after recovery, even non-
337 hospitalized patients display an increased risk of receiving a neurological or psychiatric
338 diagnoses[6], while imaging studies have revealed widespread micro-structural disruptions in a

339 subset of the recovered patients[5,6]. To a large extent, the described sequalae overlap with post-
340 infection syndromes described in patients that has recovered from infection with more
341 uncommon neuro-invasive RNA viruses, such as the West Nile virus or the Zika virus [8]. In murine
342 models for encephalitis caused by these viruses, CNS-damage continues after virus elimination[8],
343 and can be largely attributed to interferon-responsive microglia that excessively eliminate pre-
344 or post-synaptic termini as well as induce neuronal apoptosis[9,10]. Here we infect brain
345 organoids containing innately developing microglia with live SARS-CoV-2 virus and observe a
346 widespread neuronal cell death as well as a clear decrease in post-synaptic density. We show
347 that microglia in the infected organoids increase the engulfment of postsynaptic termini with a
348 concomitant upregulation of interferon-responsive genes as well as genes promoting
349 phagocytosis and synapse elimination, while neurons down-regulate 'don't-eat-me' signals.
350 Transcriptomic profiling on single cell level reveal that microglia in the infected condition
351 largely overlap with the signature of interferon-responsive microglia described in AD or PD.
352 Interestingly, these disorders are also characterized by an early synapse loss driven by
353 microglial synapse elimination[39], and the incidence is increased post COVID-19[3]. Similar,
354 microglia-mediated synapse elimination has also been observed in schizophrenia models[61],
355 another disorder that display an increased incident risk after COVID-19 infection[3].
356
357 SARS-CoV-2 infection in brain organoids also leads to secretome alterations in astrocytes,
358 pericytes and choroid plexus related cells indicating a compromised capacity to keep BBB
359 integrity, as well as an upregulation of pathways related to signaling with peripheral immune
360 cells. The murine models of Zika or West Nile encephalitis have revealed a role of infiltrating

361 $CD8^+$ T-cells to activate interferon signaling in microglia[10], then suggesting that a similar
362 mechanism could exacerbate synaptic stripping secondary to SARS-CoV-2 exposure in a model
363 that includes $CD8^+$ T-cells.
364
365 Although it is unclear to what extent the used virus loads recapitulate *in vivo* exposure, it is
366 noteworthy that we here observe the microglial responses on modest virus titers that cause a
367 limited infection of neuronal cells. While viral gene copies increase in the supernatants of
368 infected organoids, the number of PFUs promptly decrease at 72hpi. This suggests that the
369 limited number of infected cells either have an inefficient assembly and shedding of viral
370 particles, or that cell death decreases the availability of viable cells to sustain the production of
371 fully assembled viral particles.
372
373 Existing protocols for generating brain organoids have several constraints that also limit our
374 interpretations. Importantly, brain organoids most closely resemble the developing fetal brain
375 rather than the mature adult brain. Thus, we cannot exclude important differences exist in the
376 cellular responses and tropism between immature and more mature brain cells, and primarily
377 our model should be considered to recapitulate the responses to SARS-CoV-2 of the developing
378 brain. Finally, our model does not include peripheral immune cells and thus cannot capture
379 effects related to infiltrating immune cells. For example, a likely scenario is that infiltration of
380 $CD8^+$ T-cells would have amplified microglial responses. However, by excluding infiltrating
381 monocyte-derived cells, the model is optimized for assessing microglial responses thus avoiding
382 difficulties with distinguishing them from that of peripheral macrophages.

383

384 In summary, we here provide an experimental approach for modeling viral encephalitis that
385 includes tightly orchestrated responses of microglia and astrocytes in the context of neuronal
386 circuits. Challenging this model with modest live SARS-CoV-2 virus titers, we observe extensive
387 neuronal cell death and microglia-mediated synapse loss. A key next step will be to determine
388 the clinical importance of such molecular processes, and specifically whether they may
389 contribute to synapse loss and the neurocognitive and neuropsychiatric symptoms observed in
390 a subset of COVID-19 patients across different developmental stages. If so, these microglia-
391 containing organoid models may provide an opportunity to evaluate microglia-targeted
392 therapeutics aimed at minimizing or preventing these COVID-19 sequelae.

393 **MATERIALS AND METHODS**

394 *Ethics*

395 All individuals signed a written informed consent before participating in the study, as approved
396 by the Institutional Review Board of Partners HealthCare (Boston, MA, USA) and the Regional
397 Ethical Review Boards in Stockholm, Sweden. All relevant ethical regulations were followed
398 when performing the study.

399

400 *Vero E6 cells*

401 Vero E6 (ATCC-CRL-1586) cells were maintained in Dulbecco's modified eagle medium (DMEM,
402 Cytiva) supplemented with 5 % heat-inactivated fetal bovine serum (FBS, Cytiva), 100 U/mL
403 penicillin and 100 µg/mL streptomycin (Cytiva).

404

405 *iPSC reprogramming*

406 Two healthy human iPSC lines (males) were obtained from the MGH Neurobank. Briefly, iPSC
407 colonies were obtained using mRNA reprogramming in a feeder-free culture system as
408 described previously[24]. Stable iPSCs were expanded in mTESR plus media (STEMCELL
409 Technologies) and on biolaminin 521 LN-coated (BioLamina) plates. iPSCs were then purified
410 using MACS with anti-TRA-1–60 MicroBeads (Miltenyi Biotec) on LS columns. All fibroblasts and
411 iPSCs were screened and found negative for Mycoplasma and stained positive for pluripotency
412 markers like octamer-binding transcription factor 4 (POU domain, class 5, transcription factor 1)
413 and TRA-1–60.

414

415

416 *Brain organoid cultures*

417 Undirected brain organoids were prepared from single cell suspension of human iPSCs as
418 previously described[21]. Briefly, embryoid bodies (EBs) were generated by seeding 9000 single
419 cells in each well of a low attachment 96-well U-bottom plate with Y-27632 ROCK inhibitor (10
420 µM) for one day. EB media was replaced on day 5 with Neural induction media in the same 96-
421 well plate. On day 10-11, EBs were embedded in 30µl Matrigel (Corning) using sheets of
422 dimpled parafilm and incubated for 20 min at 37°C as previously detailed. Matrigel embedded
423 single EBs were then either transferred to a 24-well plate in 3ml of expansion media per well,
424 on an orbital shaker (90 rpm), or to a 12-well miniaturized bioreactor (largely overlapping with
425 the design proposed by Qian et al.)[62], until further use.

426

427 *Induced microglia-like cells*

428 iMGs were derived from monocytes (donated from one healthy male) using established
429 methods previously described in detail[23,24]. Briefly, whole blood was collected into vacutainer
430 cell preparation tubes containing sodium citrate as an anticoagulant (Becton, Dickinson and
431 Company) and processed as per the manufacturer's instructions. Peripheral blood mononuclear
432 cells (PBMC) were isolated, washed twice with PBS by centrifugation and suspended in heat-
433 inactivated fetal bovine serum (FBS; Sigma) containing 10% DMSO (Sigma). The cell suspension
434 was then divided into aliquots and cryopreserved. Generation of induced microglia-like cells
435 (iMG) from PBMCs were carried out using methods previously described[23], with minor
436 modifications. Briefly, cryopreserved PBMC samples were transferred from liquid nitrogen

437 freezer to a 37 °C water bath. Once the cell suspension had been thawed, it was gently pipetted
438 into 10 ml of pre warmed complete RPMI medium (CM) consisting of basal RPMI-1640
439 supplemented with 10% heat-inactivated FBS and 1% penicillin-streptomycin (P/S; Thermo
440 Fisher Scientific). Following centrifugation (300 *g* for 5 min at room temperature), the
441 supernatant was discarded, and the cell pellet was resuspended in the appropriate volume of
442 CM. Isolated PBMCs were cultured at a density of $5x10^5$ cells/1 ml CM on 24-well plates coated
443 with Geltrex (Thermo Fisher Scientific). After 24 h of incubation, the media was replaced with
444 RPMI-1640 supplemented with 1x glutamax (Life Technologies), 1% P/S and 0.1 $\mu g\ ml^{-1}$ of
445 interleukin (IL)-34 (R&D Systems) and 0.01 $\mu g\ ml^{-1}$ of granulocyte macrophage colony-
446 stimulating factor (GM-CSF; R&D Systems). After 7 days, fresh media was added. At day 11, cells
447 were used for infection.
448
449 *Virus isolate*
450 SARS-CoV-2 (GenBank: MT093571.1), originally from the Public Health Agency of Sweden, was
451 propagated on 90% confluent Vero E6 cells for 3 days at 37 °C. Cell debris were removed by
452 centrifugation at 300 RCF for 5 minutes and the viral supernatant was aliquoted into cryovials
453 and stored at -80 °C. Viral titers were quantified by PFU assay.
454
455 *Viral infection*
456 All experimental studies involving infectious SARS-CoV-2 were performed within the biosafety
457 level 3 (BSL3) facility at Karolinska Institute. From single cell dissociation experiments,
458 approximately $1x10^6$ cells were found to be present in a D56 organoid. Based on this, $3x10^5$

459 PFU/ml of SARS-CoV2 was used to infect organoids for 2h (such that the estimated MOI was 1
460 for periphery and 0.3 for the whole organoid) in a spinning bioreactor. Following viral
461 exposure, the organoids were washed twice with PBS and transferred into fresh medium (2ml)
462 to follow the course of infection. To monitor viral replication, 100µl of medium was collected at
463 specified time points, centrifuged at 300g for 5 min and the supernatant was collected in trizol
464 for qPCR analysis. For single cell RNA sequencing (scRNA-seq), the viral load was reduced to 1
465 $x10^5$ PFU/ml (MOI 0.1) in order to reduce the percentage of cell death observed with the
466 previous MOI.
467
468 *Plaque forming unit assay*
469 PFU assays was performed on 24-well cell culture plates seeded with $2x10^5$ Vero E6 cells per
470 well. A serial dilution of the inoculum medium (consisting of either the viral stock or
471 experimental samples in DMEM) was prepared and 200µL used to infect each well. The plates
472 were then incubated for 1 hour at 37 °C, 5% CO2. After the incubation period, the wells were
473 washed twice with PBS and 1 mL of overlay medium (2:3 mix of 3% high density carboxymethyl
474 cellulose and complete DMEM medium) was added to each well and the plates incubated for 3
475 days at 37 °C, 5% CO2. The plates were subsequently inactivated with 1 mL of 10%
476 formaldehyde solution overnight at RT, washed twice with PBS, stained with 200µL of crystal
477 violet solution for 30 min at room temperature and the plaques counted.
478
479 *Immunohistochemistry*

480 Organoids were fixed with 4% paraformaldehyde for 20 min at RT followed by 24h in 30%
481 sucrose in PBS. Organoids were then embedded in OCT (VWR) and frozen at –80°C.
482 Cryosections (16 um) of brain organoids were incubated with blocking solution for 1h (10% of
483 Normal Donkey serum in 0.3% Triton X) in 1xPBS. Blocked cryosections were incubated with the
484 respective primary antibodies, diluted in blocking solution and incubated overnight at 4°C:,
485 anti-b-III-tubulin (mouse, Promega G712A, 1:500), Cleaved caspase-3 (rabbit, Cell Signaling,
486 1:300), anti-PAX6 (mouse, Developmental Studies Hybridoma Bank, 1:100), anti-SOX10
487 antibody (goat, R&D AF2864, 1:50), anti-OLIG2 (goat, R&D AF2418, 1:100), anti-GFAP (mouse,
488 Sigma G3893, 1:100), anti-IBA1 (rabbit, Wako 019-19741, 1:100), anti-MMP14 (mouse, R&D
489 MAB918-SP, 1:100), anti-ISG15 (mouse, Santa Cruz Ltd sc166755, 1:100), anti-PSD95 (mouse,
490 Abcam 13552, 1:100), anti-PDGFRB (goat, R&D AF385-SP, 1:200), anti-LAMP2 (goat, R&D
491 AF6228-SP, 1:200) and SARS-CoV-2 (2019-nCoV) Nucleoprotein / NP Antibody (rabbit,
492 Nordicbiosite 158-40143, 1:200). Cryosections were washed three times with 1xPBS and
493 incubated with the secondary antibody for 1h at RT. Secondary antibodies (all conjugated to
494 Alexa Fluor 488, 555 and 647) were purchased from Life Technologies and used at a 1:500
495 dilution. Then, samples were washed three times with (1xPBS), incubated for 5 minutes with
496 fluorescent nuclear DAPI stain (VWR; 1:5000), and mounted with DAKO immunofluorescence
497 mounting media (Life Technologies). Image acquisition was performed using a Zeiss LSM800
498 confocal microscope (40X/1.2 W objective). Super resolution imaging acquisition was
499 performed using a Zeiss LSM900-Airy2 scan confocal microscope (63X/1.4 oil objective) for
500 representative images.
501

502 *Image quantification*

503 Immunofluorescence images were acquired using Zeiss LSM-800 confocal, LSM900-Airy2
504 (super-resolution) microscope and analyzed using CellProfiler software to measure and classify
505 cells according to the expression of the selected markers. First, the software was trained to
506 automatically segment the images into: (1) cells ($DAPI^+$ objects); (2) NP or casp3 objects,
507 followed by relating objects (1) and (2). For cell type specific quantifications, (2) was related to
508 (3) objects segmented by cell type specific markers stained by antibodies indicated above.
509 Finally, the related objects were expressed as a percentage of $DAPI^+$ cells. For validation of DE
510 genes, 40X confocal images were obtained as tiles for the whole organoid and were processed
511 in ImageJ/FIJI software (v2.1) for colocalization analyses.

512

513 For quantification of microglial engulfment of post-synaptic termini, images were acquired
514 throughout the organoid while focusing on areas with $IBA1^+$ cells (blinded to condition). The
515 images were then processed using ImageJ/FIJI software (v2.1) macro consisting of the following
516 steps: duplication of the red channel (corresponding to IBA1); background subtraction
517 (rollingball set to 20); conversion to binary image; filters set to maximum and minimum of
518 radius=5 followed by particles regarded as ROIs with size >1000 pixels. Then, for each ROI in a
519 FOV, the green channel (corresponding to PSD-95) was used to set threshold (50, 255) and
520 particles with size >3 pixels (circularity 0.01-1.00) were analyzed for number and area of each
521 synaptic puncta. Total synaptic area in a ROI was normalized by the area of the corresponding
522 ROI to get a measure of engulfment. The same set of images were used to measure area of

523 colocalization between channels corresponding to MAP2 and PSD-95, respectively, followed by
524 normalization with total MAP2 area in a FOV.
525
526
527
528 *Quantitative PCR (qPCR)*
529 RNA extraction was performed using DirectZol RNA-Miniprep Kit (Zymo Research Inc.),
530 following the manufacturer's protocol. Samples collected in TRI reagent were applied to Zymo-
531 spin columns. DNase I treatment was performed for samples with genomic DNA. Bound RNA
532 was washed, diluted in 30ul nuclease-free water and stored at -80°C. Quality and concentration
533 of extracted RNA was determined using a NanoDrop (Thermofischer Scientific). Total RNA was
534 reverse-transcribed to cDNA using the High-Capacity RNA-to-cDNA Synthesis kit (Thermofischer
535 Scientific) following manufacturer's protocol. Reverse transcription reactions were carried out
536 in 20ul reaction volume containing 1ug of input RNA with the following thermal cycler
537 conditions: 37°C (60 minutes) + 95°C (5 minutes) + 4°C (∞). cDNA was further diluted to 1:3 and
538 used as templates for PCR reactions.
539
540 PCR reactions were performed using the StepOnePlus™ Real-time PCR system (Applied
541 Biosystems, Thermofischer Scientific) with PowerTrack™ SYBR Green Master Mix. Expression of
542 viral mRNA was assessed by evaluating threshold cycle (Ct) values. Relative expression levels of
543 N gene in cell lysates were normalized against a housekeeping gene, GAPDH (glyceraldehyde-3-
544 phosphate dehydrogenase), according to the Delta delta Ct method. Absolute quantification of

545 viral gene expression levels in the supernatant were performed using the standard curve
546 method. Primer sequences used in this study are:
547 GAPDH Forward – GGTGGTCTCCTCTGACTTCAACA
548 GAPDH Reverse – GTGGTCGTTGAGGGCAATG
549 N gene Forward – CATTGGCATGGAAGTCACAC
550 N gene Reverse – TCTGCGGTAAGGCTTGAGTT
551 RdRp Forward – CGCATACAGTCTTRCAGGCT
552 RdRp Reverse – GTGTGATGTTGAWATGACATGGTC
553 *Dissociations for single cell RNA sequencing*
554 Briefly, three organoids per condition (control, 24hpi, 72hpi) were washed twice with DPBS
555 without ions and cut into small pieces using a sterile scalpel. Single cell suspension was
556 generated using neural dissociation kit (Miltenyi Biotec) according to manufacturer's protocol.
557 Microglia was enriched using CD11b magnetic microbeads (Miltentyi Biotec) using MACS.
558 Viability and cell numbers were assessed for both MACS-enriched and flow-through fractions
559 before proceeding with the 10X protocol.
560
561 *Single-cell RNA-sequencing*
562 Two single cell suspensions per condition were loaded onto a single Chromium controller chip
563 v3.1 (10X Genomics), with a target output of 6000-7000 cells per channel. For the six loaded
564 channels, GEM generation, barcoding, cDNA amplification and library preparation was
565 performed using the Single-cell 3' Gel Bead and Library v3.1 kit (10X Genomics) at the
566 Eukaryotic Single Cell Genomics facility (SciLifeLab, Sweden). Amplified cDNA and final libraries

567 were evaluated on a Bioanalyzer for quality control and sequenced together on Illumina
568 NovaSeq 6000 platform.
569
570
571
572 *Data processing*
573 Sequenced data was processed through the CellRanger Software (5.0 ,10X Genomics) and
574 transcripts were aligned to a combined reference of Human GRCh38-3.0.0 and SARS-Cov-2
575 genome (GenBank: MT093571.1). Filtered feature-barcode matrices from CellRanger were
576 further subjected to quality control measures where low-quality cells with < 200 uniquely
577 expressed genes and high percentage of mitochondrial reads (>20%) were filtered out.
578 Doublets were identified using scDblFinder package[63] and removed with caution. Genes
579 expressed in fewer than 5 cells were filtered out. Filtered count matrices were merged and
580 analyzed downstream using the Seurat package[64]. Expression data per experimental condition
581 was normalized using the regularized negative binomial regression method implemented in
582 SCTransform[65], while regressing out the difference between the G2M and S phase scores, which
583 served as a confounding factor in our dataset. Anchors across conditions were identified using
584 FindIntegrationAnchors function and samples were integrated using canonical correlation
585 analysis (CCA) implemented in the IntegrateData function of Seurat. Linear data compression
586 using principal component analysis (PCA) was performed on 3000 highly variable genes. Top 30
587 PCs were used as the input to perform non-linear dimensionality reduction using UMAP.
588

589 *Clustering and cell-type identification*

590 We constructed a k-nearest neighbor (KNN) graph based on Euclidean distance in 30 PCs and
591 performed unsupervised graph-based clustering using the Louvain algorithm (modularity
592 resolution = 0.8) with functions provided in Seurat. Preliminary clustering of 39,808 cells
593 identified 21 clusters yielding a clear separation of neuro-ectodermal clusters. Non-
594 neuroectodermal clusters that did not express known marker genes related to cell types
595 present in the brain, were removed. The remaining 26,148 cells were then subjected to second-
596 level clustering in an integrated space (resolution= 0.6), yielding 16 final clusters. The clustering
597 was visualized using UMAP embedding in two dimensions. Top differentially expressed genes
598 conserved across conditions for the final clusters were identified using a non-parametric
599 Wilcoxon rank-sum test in FindConservedMarkers function. P-values were adjusted based on
600 Bonferroni correction and genes with at least 25% cluster-specific expression, >0.25 average
601 log-fold change, and FDR<0.01 were chosen to identify the clusters. All cells were assigned
602 scores based on cell type-specific gene modules to further identify broad cell types such as
603 neurons, astrocytes, microglia and oligodendrocytes. A priori set of markers curated based on
604 previous studies of cerebral organoids and developing fetal brain was explored to manually
605 annotate the clusters. Additionally, we leveraged existing published fetal brain and organoid
606 scRNA-seq datasets and undertook a correlation-based method[66] (Spearman) to compare our
607 annotated clusters to transcriptional profiles of previously annotated cell types.

608

609 *Differential expression testing and functional interpretation*

610 We performed differential gene expression analyses on each cluster across conditions on log-
611 normalized values using the MAST package[67] in R. DEGs were considered significant if their
612 Benjamini-Hochberg-adjusted P-value was < 0.05 and a log2 fold change was > 0.25. Significant
613 DEGs were used to perform GO term overrepresentation analysis using the enrichR package.
614 Gene set enrichment analysis (GSEA) was performed on ranked DEGs using fgsea package[68] for
615 pathway analysis (KEGG, GO:BPdatabase). Gene sets were limited by minSize=3 and
616 nPerm=10000. Normalized enrichment scores were calculated and plotted for pathways with
617 adjusted p-values < 0.05. Statistical significance of association of DEGs with gene signatures
618 from published datasets was performed using Fischer's exact test to obtain a p-value (<0.05,
619 adjusted with BH method) and Odds ratio (OR). Number of genes expressed in the respective
620 cell type was used as the genomic background.

621 *Intercellular interaction*

622 Cellular crosstalk was inferred via ligand-receptor pair expression using CellphoneDB package[69]
623 (v2) in python. Statistical analysis was performed within the package with default parameters
624 (1000 iterations) and no subsampling was done.

625

626 *Statistics*

627 The assumptions of each used test were checked. All reported p-values are two sided and type
628 of statistical test is reported in the figure legends or in the main text.

629

630 **DATA AND CODE AVAILABILITY**

631 Processing of data and downstream analysis was performed in R (version 4.0.3). Figures used in
632 this manuscript were generated in Python (version 3.6.12). Raw single-cell RNA sequencing data
633 is deposited into GEO database (GSE181422). Source code to reproduce the findings are
634 available in our repository on Github (https://github.com/SellgrenLab/organoid-Covid19). All
635 other data is available from the corresponding authors upon request.

REFERENCES

1. Ellul, M. A. *et al.* Neurological associations of COVID-19. *The Lancet. Neurology* **19**, 767–783 (2020).
2. Matschke, J. *et al.* Neuropathology of patients with COVID-19 in Germany: a post-mortem case series. *The Lancet. Neurology* **19**, 919–929 (2020).
3. Taquet, M., Geddes, J. R., Husain, M., Luciano, S. & Harrison, P. J. 6-month neurological and psychiatric outcomes in 236 379 survivors of COVID-19: a retrospective cohort study using electronic health records. *The Lancet Psychiatry* **8**, 416–427 (2021).
4. Perlis, R. H. *et al.* Comparison of post-COVID depression and major depressive disorder. *medRxiv: the preprint server for health sciences* (2021) doi:10.1101/2021.03.26.21254425.
5. Lu, Y. *et al.* Cerebral Micro-Structural Changes in COVID-19 Patients - An MRI-based 3-month Follow-up Study. *EClinicalMedicine* **25**, 100484 (2020).
6. Garrigues, E. *et al.* Post-discharge persistent symptoms and health-related quality of life after hospitalization for COVID-19. *The Journal of infection* **81**, e4–e6 (2020).
7. Al-Aly, Z., Xie, Y. & Bowe, B. High-dimensional characterization of post-acute sequelae of COVID-19. *Nature* **594**, 259–264 (2021).
8. Chhatbar, C. & Prinz, M. The roles of microglia in viral encephalitis: from sensome to therapeutic targeting. *Cellular & molecular immunology* **18**, 250–258 (2021).
9. Vasek, M. J. *et al.* A complement–microglial axis drives synapse loss during virus-induced memory impairment. *Nature* **534**, 538–543 (2016).
10. Garber, C. *et al.* T cells promote microglia-mediated synaptic elimination and cognitive dysfunction during recovery from neuropathogenic flaviviruses. *Nature neuroscience* **22**, 1276–1288 (2019).
11. van den Pol, A. N. Viral infections in the developing and mature brain. *Trends in neurosciences* **29**, 398–406 (2006).
12. Cugola, F. R. *et al.* The Brazilian Zika virus strain causes birth defects in experimental models. *Nature* **534**, 267–271 (2016).
13. Brain Region-specific Organoids using Mini-bioreactors for Modeling ZIKV Exposure HHS Public Access. **165**, 1238–1254 (2016).
14. Ramani, A. *et al.* <scp>SARS</scp> -CoV-2 targets neurons of 3D human brain organoids. *The EMBO Journal* **39**, (2020).
15. Jacob, F. *et al.* Human Pluripotent Stem Cell-Derived Neural Cells and Brain Organoids Reveal SARS-CoV-2 Neurotropism Predominates in Choroid Plexus Epithelium. *Cell stem cell* (2020) doi:10.1016/j.stem.2020.09.016.
16. Zhang, B. Z. *et al.* SARS-CoV-2 infects human neural progenitor cells and brain organoids. *Cell Research* 1–4 (2020) doi:10.1038/s41422-020-0390-x.
17. Song, E. *et al.* Neuroinvasion of SARS-CoV-2 in human and mouse brain. *Journal of Experimental Medicine* **218**, (2021).
18. Pellegrini, L. *et al.* SARS-CoV-2 Infects the Brain Choroid Plexus and Disrupts the Blood-CSF Barrier in Human Brain Organoids. *Cell stem cell* **27**, 951-961.e5 (2020).
19. Schulz, C. *et al.* A lineage of myeloid cells independent of myb and hematopoietic stem cells. *Science* **335**, 86–90 (2012).

679 20. Ginhoux, F. *et al.* Fate mapping analysis reveals that adult microglia derive from primitive
680 macrophages. *Science* **330**, 841–845 (2010).
681 21. Ormel, P. R. *et al.* Microglia innately develop within cerebral organoids. *Nature*
682 *communications* **9**, 4167 (2018).
683 22. Bennett, M. L. *et al.* New tools for studying microglia in the mouse and human CNS.
684 *Proceedings of the National Academy of Sciences of the United States of America* **113**,
685 E1738-46 (2016).
686 23. Sellgren, C. M. *et al.* Patient-specific models of microglia-mediated engulfment of
687 synapses and neural progenitors. *Molecular Psychiatry* **22**, 170–177 (2017).
688 24. Sellgren, C. M. *et al.* Increased synapse elimination by microglia in schizophrenia patient-
689 derived models of synaptic pruning. *Nature Neuroscience* **22**, 374–385 (2019).
690 25. Nowakowski, T. J. *et al.* Spatiotemporal gene expression trajectories reveal
691 developmental hierarchies of the human cortex. *Science* **358**, (2017).
692 26. Pollen, A. A. *et al.* Molecular Identity of Human Outer Radial Glia during Cortical
693 Development. *Cell* **163**, (2015).
694 27. McKenzie, A. T. *et al.* Brain Cell Type Specific Gene Expression and Co-expression
695 Network Architectures. *Scientific Reports* **8**, (2018).
696 28. Vanlandewijck, M. *et al.* A molecular atlas of cell types and zonation in the brain
697 vasculature. *Nature* **554**, (2018).
698 29. Zhong, S. *et al.* A single-cell RNA-seq survey of the developmental landscape of the
699 human prefrontal cortex. *Nature* **555**, (2018).
700 30. Hodge, R. D. *et al.* Conserved cell types with divergent features in human versus mouse
701 cortex. *Nature* **573**, (2019).
702 31. Bhaduri, A. *et al.* Cell stress in cortical organoids impairs molecular subtype specification.
703 *Nature* **578**, 142–148 (2020).
704 32. Tanaka, Y., Cakir, B., Xiang, Y., Sullivan, G. J. & Park, I. H. Synthetic Analyses of Single-Cell
705 Transcriptomes from Multiple Brain Organoids and Fetal Brain. *Cell Reports* **30**, (2020).
706 33. Pollen, A. A. *et al.* Establishing Cerebral Organoids as Models of Human-Specific Brain
707 Evolution. *Cell* **176**, (2019).
708 34. Pellegrini, L. *et al.* Human CNS barrier-forming organoids with cerebrospinal fluid
709 production. *Science* **369**, (2020).
710 35. Chen, R. *et al.* The Spatial and Cell-Type Distribution of SARS-CoV-2 Receptor ACE2 in the
711 Human and Mouse Brains. *Frontiers in neurology* **11**, 573095 (2020).
712 36. Johnson, B. A. *et al.* Loss of furin cleavage site attenuates SARS-CoV-2 pathogenesis.
713 *Nature* **591**, 293–299 (2021).
714 37. Hoffmann, M. *et al.* SARS-CoV-2 Cell Entry Depends on ACE2 and TMPRSS2 and Is Blocked
715 by a Clinically Proven Protease Inhibitor. *Cell* **181**, 271-280.e8 (2020).
716 38. Guo, H., Callaway, J. B. & Ting, J. P. Y. Inflammasomes: Mechanism of action, role in
717 disease, and therapeutics. *Nature Medicine* vol. 21 677–687 (2015).
718 39. Henstridge, C. M., Tzioras, M. & Paolicelli, R. C. Glial Contribution to Excitatory and
719 Inhibitory Synapse Loss in Neurodegeneration. *Frontiers in Cellular Neuroscience* **13**,
720 (2019).

721 40. Sala Frigerio, C. *et al.* The Major Risk Factors for Alzheimer's Disease: Age, Sex, and
722 Genes Modulate the Microglia Response to Aβ Plaques. *Cell Reports* **27**, 1293-1306.e6
723 (2019).
724 41. Hammond, T. R. *et al.* Single-Cell RNA Sequencing of Microglia throughout the Mouse
725 Lifespan and in the Injured Brain Reveals Complex Cell-State Changes. *Immunity* **50**, 253-
726 271.e6 (2019).
727 42. Keren-Shaul, H. *et al.* A Unique Microglia Type Associated with Restricting Development
728 of Alzheimer's Disease. *Cell* **169**, 1276-1290.e17 (2017).
729 43. Olah, M. *et al.* Single cell RNA sequencing of human microglia uncovers a subset
730 associated with Alzheimer's disease. *Nature Communications* **11**, 1–18 (2020).
731 44. Ohsawa, K., Imai, Y., Sasaki, Y. & Kohsaka, S. Microglia/macrophage-specific protein Iba1
732 binds to fimbrin and enhances its actin-bundling activity. *Journal of Neurochemistry* **88**,
733 844–856 (2004).
734 45. Gardai, S. J. *et al.* Cell-surface calreticulin initiates clearance of viable or apoptotic cells
735 through trans-activation of LRP on the phagocyte. *Cell* **123**, 321–334 (2005).
736 46. Schaer, D. J., Alayash, A. I. & Buehler, P. W. Gating the radical hemoglobin to
737 macrophages: The anti-inflammatory role of CD163, a scavenger receptor. *Antioxidants
738 and Redox Signaling* vol. 9 991–999 (2007).
739 47. Gold, L. I. *et al.* Calreticulin: non-endoplasmic reticulum functions in physiology and
740 disease. *The FASEB Journal* **24**, 665–683 (2010).
741 48. Canton, J., Neculai, D. & Grinstein, S. Scavenger receptors in homeostasis and immunity.
742 *Nature Reviews Immunology* vol. 13 621–634 (2013).
743 49. Józefowski, S. & Kobzik, L. Scavenger receptor A mediates H 2 O 2 production and
744 suppression of IL-12 release in murine macrophages . *Journal of Leukocyte Biology* **76**,
745 1066–1074 (2004).
746 50. O'Callaghan, J. P., Kelly, K. A., VanGilder, R. L., Sofroniew, M. V. & Miller, D. B. Early
747 activation of STAT3 regulates reactive astrogliosis induced by diverse forms of
748 neurotoxicity. *PLoS ONE* **9**, 102003 (2014).
749 51. Sofroniew, M. V. Astrocyte Reactivity: Subtypes, States, and Functions in CNS Innate
750 Immunity. *Trends in Immunology* vol. 41 758–770 (2020).
751 52. Barbar, L. *et al.* CD49f Is a Novel Marker of Functional and Reactive Human iPSC-Derived
752 Astrocytes. *Neuron* **107**, 436-453.e12 (2020).
753 53. Al-Dalahmah, O. *et al.* Single-nucleus RNA-seq identifies Huntington disease astrocyte
754 states. *Acta Neuropathologica Communications* **8**, 1–21 (2020).
755 54. Chen, Z. & Li, G. Immune response and blood–brain barrier dysfunction during viral
756 neuroinvasion. *Innate Immunity* **27**, 109–117 (2021).
757 55. Zhang, K. & Kaufman, R. J. Signaling the unfolded protein response from the endoplasmic
758 reticulum. *Journal of Biological Chemistry* vol. 279 25935–25938 (2004).
759 56. Poljsak, B., Šuput, D. & Milisav, I. Achieving the balance between ROS and antioxidants:
760 When to use the synthetic antioxidants. *Oxidative Medicine and Cellular Longevity* (2013)
761 doi:10.1155/2013/956792.
762 57. Ana Campos Codo, A. *et al.* Elevated Glucose Levels Favor SARS-CoV-2 Infection and
763 Monocyte Response through a HIF-1a/ Glycolysis-Dependent Axis II Elevated Glucose

764 Levels Favor SARS-CoV-2 Infection and Monocyte Response through a HIF-1a/Glycolysis-
765 Dependent Axis. *Cell Metabolism* **32**, 437-446.e5 (2020).
766 58. Stoolman, J. S. & Chandel, N. S. Glucose Metabolism Linked to Antiviral Responses. *Cell*
767 vol. 178 10–11 (2019).
768 59. Weber, B. & Barros, L. F. The astrocyte: Powerhouse and recycling center. *Cold Spring*
769 *Harbor Perspectives in Biology* **7**, 20396–20397 (2015).
770 60. Taquet, M., Geddes, J. R., Husain, M., Luciano, S. & Harrison, P. J. 6-month neurological
771 and psychiatric outcomes in 236379 survivors of COVID-19: a retrospective cohort study
772 using electronic health records. *The lancet. Psychiatry* **8**, 416–427 (2021).
773 61. Sellgren, C. M. *et al.* Increased synapse elimination by microglia in schizophrenia patient-
774 derived models of synaptic pruning. *Nature Neuroscience* **22**, 374–385 (2019).
775 62. Qian, X. *et al.* Generation of human brain region–specific organoids using a miniaturized
776 spinning bioreactor. *Nature Protocols* **13**, 565–580 (2018).
777 63. Germain, P.-L., Lun, A., Macnair, W. & Robinson, M. D. Doublet identification in single-
778 cell sequencing data using scDblFinder. *F1000Research* **10**, (2021).
779 64. Stuart, T. *et al.* Comprehensive Integration of Single-Cell Data. *Cell* **177**, (2019).
780 65. Hafemeister, C. & Satija, R. Normalization and variance stabilization of single-cell RNA-
781 seq data using regularized negative binomial regression. *Genome Biology* **20**, (2019).
782 66. Fu, R. *et al.* clustifyr: an R package for automated single-cell RNA sequencing cluster
783 classification. *F1000Research* **9**, (2020).
784 67. Finak, G. *et al.* MAST: a flexible statistical framework for assessing transcriptional
785 changes and characterizing heterogeneity in single-cell RNA sequencing data. *Genome*
786 *Biology* **16**, (2015).
787 68. Sergushichev A. An algorithm for fast preranked gene set enrichment analysis using
788 cumulative statistic calculation. (2016).
789 69. Efremova, M., Vento-Tormo, M., Teichmann, S. A. & Vento-Tormo, R. CellPhoneDB:
790 inferring cell–cell communication from combined expression of multi-subunit ligand–
791 receptor complexes. *Nature Protocols* **15**, (2020).
792
793

794 **ACKNOWLEDGEMENT**

795 We thank the study participants. We are also grateful to the participant core facilities at
796 Karolinska Institutet; The Biosafety Level (BSL)-3 laboratory at Biomedicum, BIC, and SciLife Lab.
797 We are thankful to Judit Ozsvar, an intern at the Sellgren laboratory at time of the experiments,
798 for her help with cell culture work, as well as to Gretchen Majkowitz for valuable feedback on
799 the manuscript. This work was supported by grants from Hjärnfonden postdoktorala stipendier
800 (S.: PS2019-0063), the Swedish Research Council (C.M.S.: 2017-02559), Karolinska Institutet
801 (C.M.S.: KID), regional agreement on medical training and clinical research between Stockholm
802 County Council (A.L.F, C.M.S.), One Mind Foundation/Kaiser Permanente (C.M.S.), and
803 Marianne and Marcus Wallenberg Foundation (C.M.S.).

804

805 **AUTHOR CONTRIBUTIONS**

806 C.M.S, S, A.O.O, S.K.G, and S.M conceived the project. R.H.P and S.D.S provided iPSCs. A.O.O
807 derived the organoids. N.R.S and S performed infections, dissociations and related assays,
808 supervised by A.R, with help from L.S. A.O.O, S, S.M optimized and performed IHCs, imaging
809 and quantifications, with help from J.G.L . S.K.G optimized the qPCR assays and performed them
810 with S.M. F.O derived microglia for 2D assays. S.M designed the scRNA-seq experiments with
811 inputs from S and C.M.S. S.M analyzed scRNA-seq data. S and S.M interpreted the data. S, S.M,
812 M.S, and C.M.S wrote the manuscript with inputs from the other co-authors.

813

814 **COMPETING INTEREST**

815 The authors declare no competing interests.

816

817 **FIGURE LEGENDS**

818 **Figure 1 Cellular composition of DIV 56 brain organoids containing innately developing**
819 **microglia** (a) Schematic of brain organoid generation using an undirected protocol adapted
820 from Ormel et al., (b) IHC staining of different cell type markers showing the presence of NPCs
821 (PAX6), immature and mature neurons (B-III Tubulin and MAP2), schwann cells (SOX10),
822 astrocytic lineage cells (GFAP, S100B) and microglia (IBA1, CD68).

823

824 **Figure 2 SARS-CoV-2 infection of immunocompetent brain organoids.** Brain
825 organoids infected with live SARS-CoV-2 virus was collected at different time points following
826 exposure. **(a)** qPCR analyses on supernatants of infected brain organoids at 56 DIV (n=3,
827 black circle) and 110 DIV (n=3, magenta circle) showing log fold change in viral nucleocapsid (*N)*
828 gene copies, at different time points. Error bars indicate standard errors of the mean (SEM).
829 **(b)** Log transformed PFUs of supernatants from infected brain organoids at different time
830 points. Error bars indicate SEM. Representative IHC tiled images showing staining of **(c)**
831 nucleocapsid protein (NP) and **(d)** cleaved caspase 3 (CASP3) in 56 DIV infected brain organoids
832 and uninfected control organoids. **(e)** Postsynaptic density (PSD-95) decreased by 50% in
833 organoids at 72hpi (Mann-Whitney U-test: P=0.025). Images are representative for each
834 condition. In the graph, bars display medians, and the data is normalized to median uptake in
835 control organoids (n=3 organoids per condition). Each data point represents the mean of all
836 cells per field of view.

837

838

839 **Figure 3 Cell type specific SARS-CoV-2 infection in brain organoids with innately developing**
840 **microglia.** 40X representative confocal images showing colocalization of viral NP
841 with **(a)** neuronal precursors (PAX6), **(b)** neurons (MAP2), and a heterogenous population of
842 progenitors marked by **(c)** GFAP **(d)** OLIG2 and **(e)** schwann cells (SOX10). **(f)** Distribution of
843 NP^+ cells amongst different cell-type markers, expressed as percentage of DAPI from two D56
844 infected organoids (corresponding data points indicated by circles and triangles). Each data
845 point is an average of 4 FOVs representing different areas on the same section. Error bars
846 indicate SEM. **(g)** 40X confocal image showing colocalization of dsRNA (for viral presence) with
847 organoid grown microglia (IBA1) and **(h)** qPCR on cell lysate fractions obtained after magnetic
848 cell sorting (MACS) with CD11b beads, (also shown A2B5 radial glia enriched fraction) and
849 flowthrough (FT), on infected organoids (n=2, pooled) showing presence of viral N gene copies.
850
851 **Figure 4. Figure Microglial engulfment of synaptic material in response to SARS-CoV-2**
852 **exposure.** Super resolution imaging showing **(a)** microglial processes ($IBA1^+$) in proximity to
853 neurons ($MAP2^+$), engulfing post-synaptic material ($PSD95^+$) with orthogonal projections
854 showing PSD95 overlapping with IBA1 **(b)** 3D reconstruction and surface rendering
855 demonstrating volumes of $PSD\text{-}95^+$ puncta inside $Iba1^+$ cells. **(c)** postsynaptic material ($PSD95^+$)
856 colocalizing with lysosome associated membrane protein, LAMP2, within phagocyting microglia
857 ($IBA1^+$). **(d)** Microglial engulfment of post-synaptic material ($PSD\text{-}95^+$) in organoids at 72hpi is
858 increased threefold (Mann-Whitney *U*-test: $P<0.0001$). Images are representative for each
859 condition. In the graph, bars display medians, and the data is normalized to median uptake in

860 control organoids (n=3 organoids per condition). Each data point represents the mean of all
861 cells per field of view.
862
863 **Figure 5. Single cell transcriptome profiling of brain organoids with innately developing**
864 **microglia.** Brain organoids (n=3) per experimental condition (control, 24 and 72hpi) were
865 dissociated into whole-cell suspensions and single cell RNA sequencing libraries were generated
866 using the droplet-based 10X platform. **(a)** UMAP plot of integrated dataset
867 containing 25336 single cells from all three conditions depicting the presence of key
868 neurodevelopmental cell types. Individual dots representing single cells are colored by the
869 identified cell type. **(b)** Cell type classification obtained by scoring cells by their expression of
870 known individual cell type signatures (**Supplementary table 1**) plotted as estimated joint
871 density on a UMAP.(c) UMAP plot of overall embedding of cells colored by the experimental
872 condition (top) and cell cycle phase (bottom) (**d)** Heatmap showing expression of top-
873 differentially expressed markers (rows) across all clusters (columns) (BH adjusted pvalue<0.05).
874 A list of all differentially expressed genes conserved across conditions for each cluster is
875 provided in supplementary table1.
876
877 **Figure 6. Expression of SARS-CoV-2 entry factors in brain organoids and microglial responses**
878 **to SARS-CoV-2. (a)** Heatmap showing relative mRNA expression levels of proposed cellular
879 entry factors utilized by SARS-CoV-2 virus across cell types. **(b)** Modules of genes with similar
880 expression behavior across conditions in microglia identified by pseudo-bulk differential gene
881 expression analysis (using LRT implemented in DESeq2). **(c)** Protein-protein interaction (PPI)

882 network of genes belonging to module A using STRING database with the top Gene Ontology
883 term identified as 'Type I interferon response' (Adjusted p-value<0.05).(d) IHC staining
884 validating ISG15 expression in control and 72hpi organoid. Quantifications provided in
885 supplementary fig 5j **(e)** Dot plot showing expression levels of neuro-immune related genes
886 such as cytokines & chemokines, interferon-stimulated genes, and their upstream effector
887 molecules across infected conditions for each cell type [24- 24 hpi; 72- 72 hpi]. Color scale
888 represents average log-scaled expression values across all cells, in each cluster. Size of the dot
889 represents the percentage of cells in each cluster, expressing the gene. **(f)** Venn diagram of
890 genes overlapping between gene signatures of Disease-associated microglia (DAM), injury-
891 associated microglia (IRM) and SARS-CoV-2 infected microglia at 72hpi (* BH adjusted p-value <
892 0.005). **(g)** Heatmap of comparisons between SARS-CoV-2-associated microglia at 24hpi & 72hpi
893 along with 9 human microglial clusters defined by *Olah et al., 2020,* colored by odds ratio (with
894 p-values shown in red) from hypergeometric gene overlap testing (Fischer's exact test,
895 Bonferroni correction, adjusted p-value<0.05). Transcriptomic gene signatures were defined as
896 differentially upregulated genes with log2FC > 0.25 and FDR<5%. **(h)** Heatmap showing gene set
897 enrichment analyses (*MSigDB* GO:BP gene sets) of differentially expressed genes (DEGs) from
898 24hpi versus control (left) and 72hpi versus control (right) for each cell type. Pathways
899 commonly dysregulated across most cell types were selected. All significantly altered pathways
900 for individual cell types are listed in Supplementary table 2 (FDR<5%, Benjamini-
901 Hochberg (BH) correction, NES- Normalized Enrichment Score).
902

903 **Figure 7. Temporal heterogeneity in astrocytes and choroid plexus responses to SARS-CoV-**
904 **2. (a)** Differential expression analysis of SARS-CoV-2 exposed astrocytes versus control
905 astrocytes, highlighted DEGs in a heatmap with top implicated pathways using
906 overrepresentation test (FDR<0.05, Benjamini-Hochberg correction; Scale bar- Log2fold change
907 values). **(b)** Cells belonging to the astrocyte cluster, as shown in Fig 4A, were extracted and
908 subjected to further unsupervised clustering. UMAP plot of astrocytes shows 6 unique
909 subclusters (AS-0, AS-2, AS-2, AS-3, AS-4 & AS-5; left) with cells colored by condition (middle)
910 and cell cycle phase (right) (clustering was performed upon regressing cell cycle effects). Each
911 dot represents a single cell colored by the respective groups shown on the right side of each
912 plot. (**c**) Dot plot of scaled average expression of genes involved in astrocytic engulfment across
913 astrocyte subclusters (adjusted P<0.05) **(d)** UMAP plot of single-cell transcriptomic data of
914 human iPSC-derived A1-astrocytes from *Barbar et al., 2020,* integrated with astrocytes from our
915 study using canonical-correlation based-approach (CCA) (implemented in Seurat). Cells are
916 colored by their respective dataset and experimental condition. **(e)** Average-scaled expression
917 of genes related to blood-brain-barrier integrity and function for different cell type clusters
918 across control and infected conditions. **(f)** IHC staining and corresponding quantification
919 validating increased MMP14 expression in $GFAP^+$ cells and **(i)** $PDGFRB^+$ cells. **(g)** Mapping
920 intercellular interactions across cell types upon infection. Heatmap showing changes in the
921 number of interactions between cell types at 24hpi (left) and 72hpi (right) resulting from SARS-
922 CoV-2 infection. Ligand-receptor interactions were inferred in the single-cell transcriptomic
923 data using *CellphoneDB*. Green depicts a negative difference indicating loss of interactions
924 whereas purple depicts a positive change indicating gain of interactions between the cell type

925 pair when compared to the control. **(h)** UMAP plot of all Choroid plexus cells colored by their

926 identified subclusters (left) and experimental condition (right).

Figure 1

a.

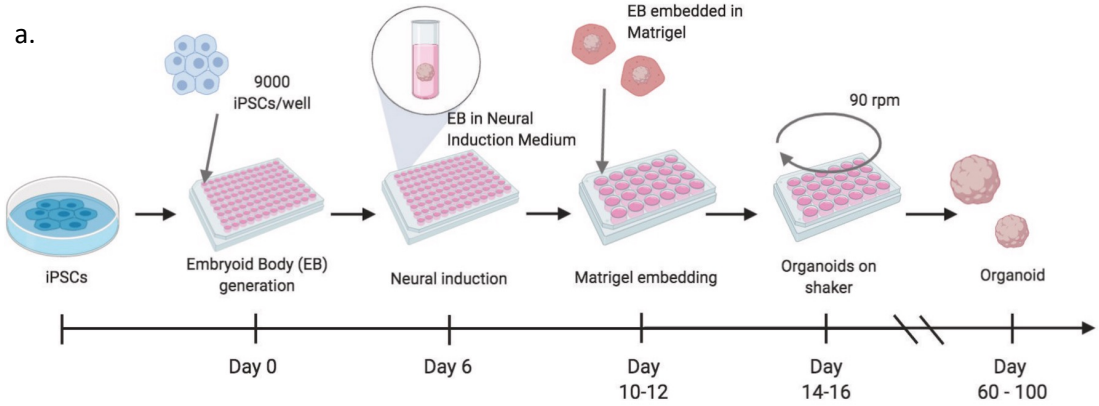
9000
iPSCs/well
EB in Neural
Induction Medium
EB embedded in
Matrigel
90 rpm
iPSCs
Embryoid Body (EB)
generation
Neural induction
Matrigel embedding
Organoids on
shaker
Organoid
Day 0
Day 6
Day
10-12
Day
14-16
Day
60 - 100

b.

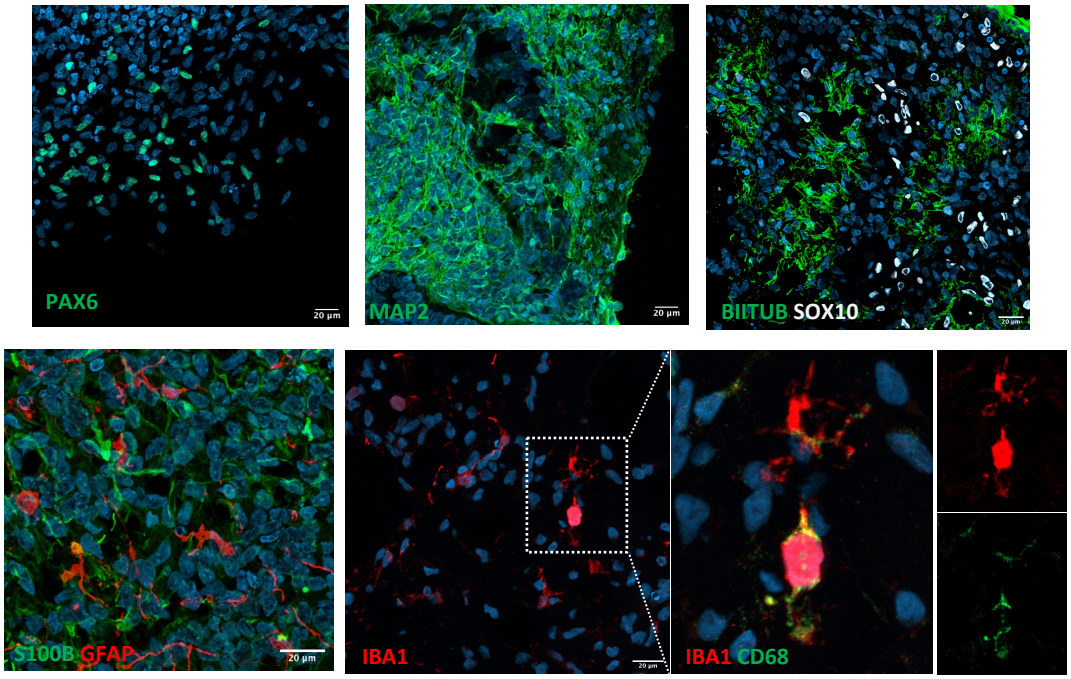
PAX6
MAP2
BIITUB SOX10
S100B GFAP
IBA1
IBA1 CD68

Figure 2

a.

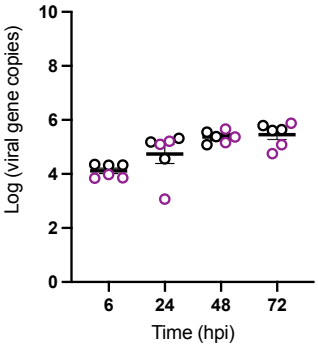

b.

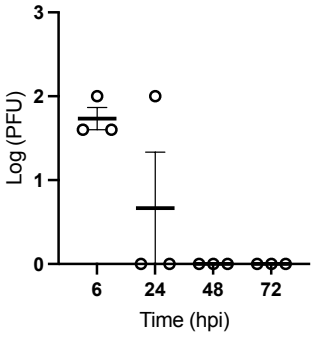

c.

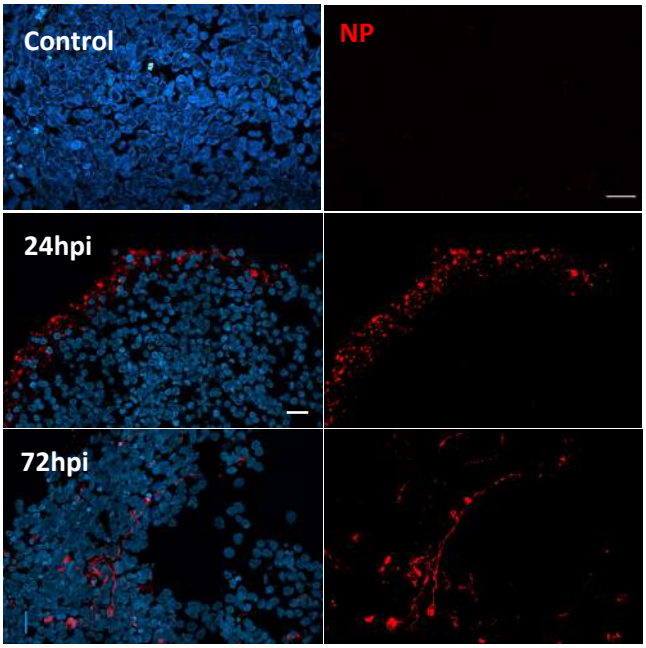

e.

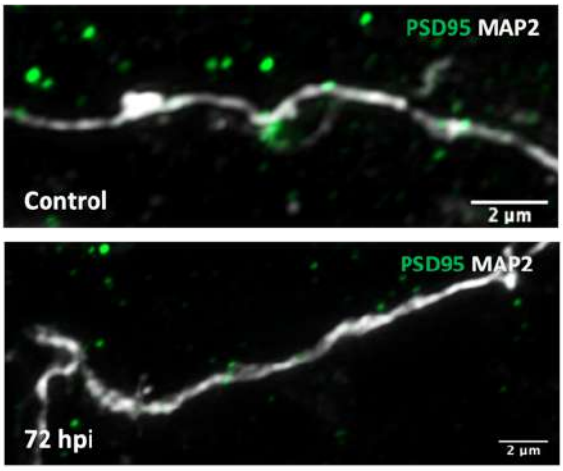

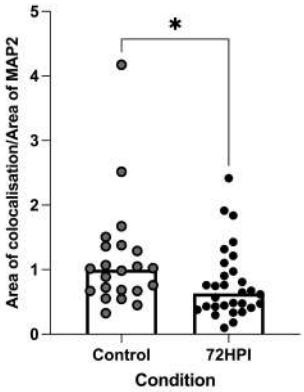

d.

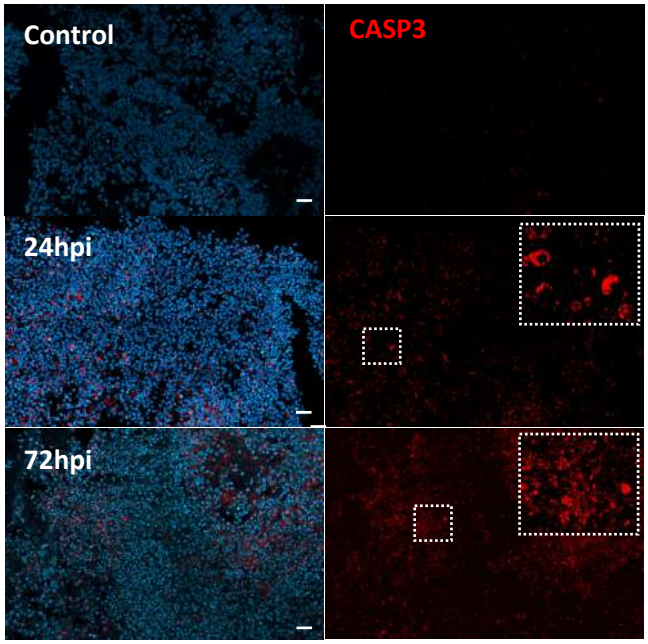

Figure 3

a.

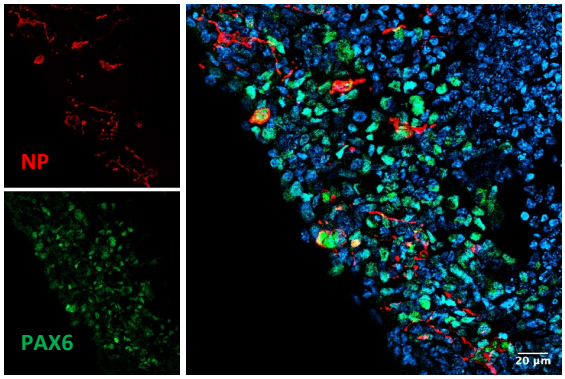

b.

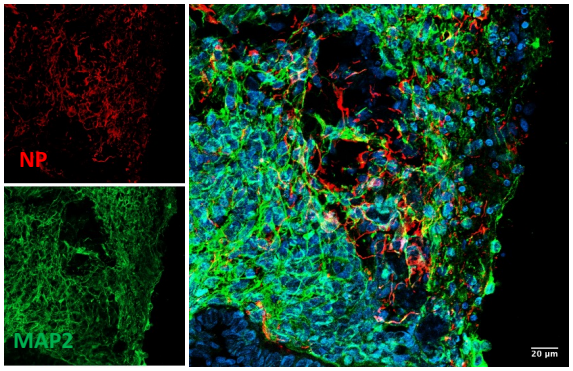

c.

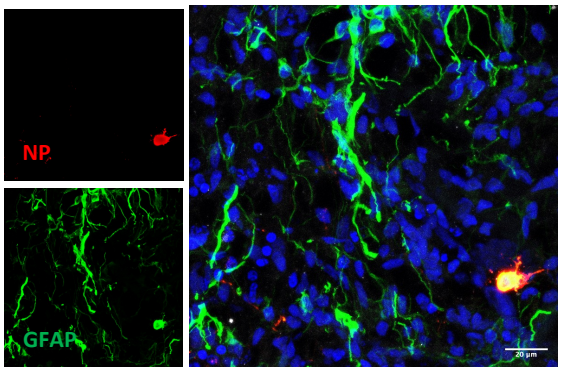

d.

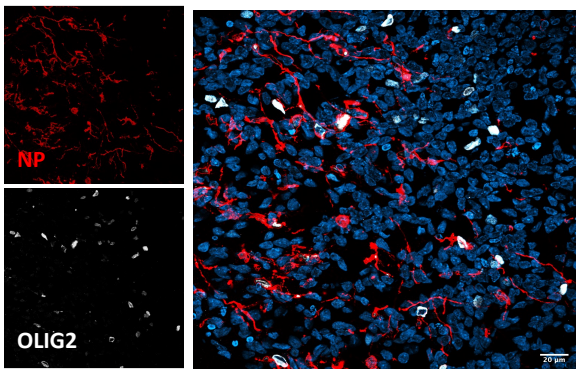

e.

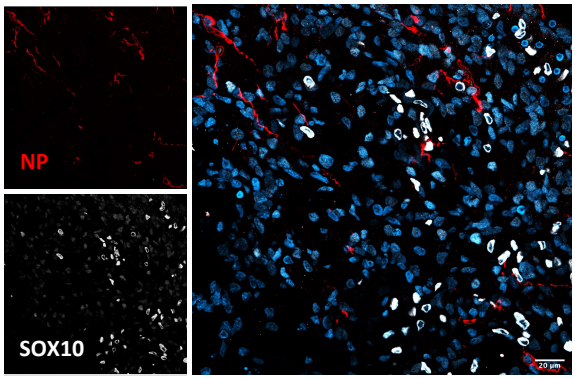

f.

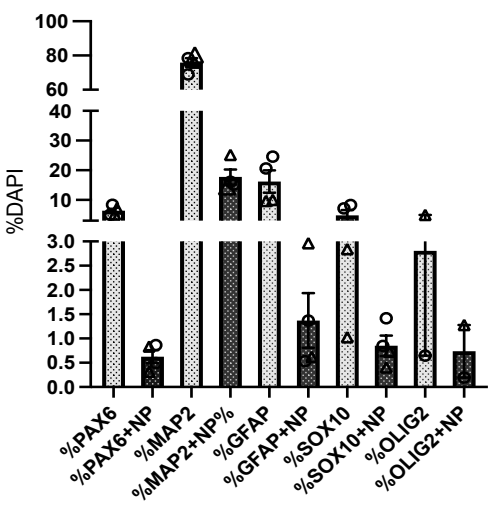

g.

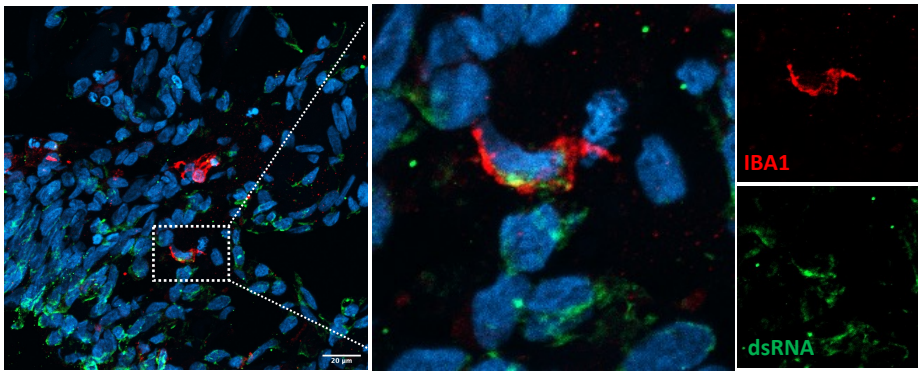

h.

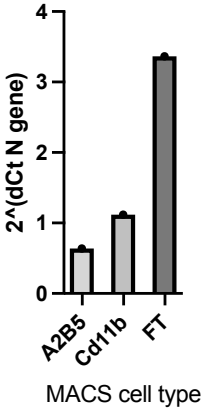

a.

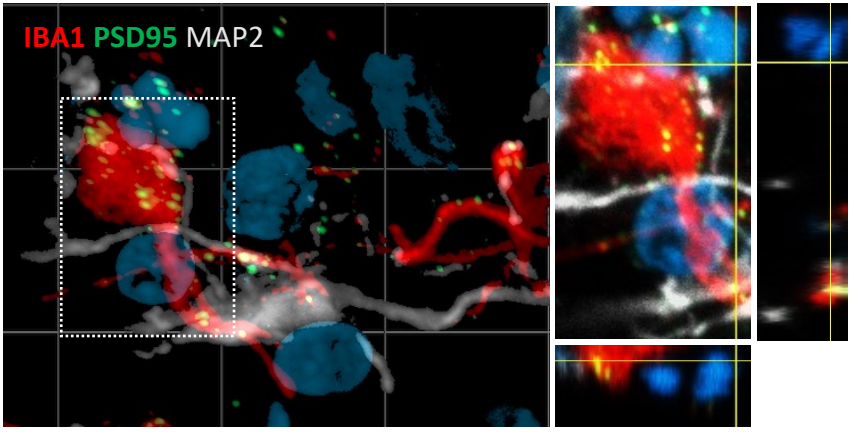
IBA1 PSD95 MAP2

b.

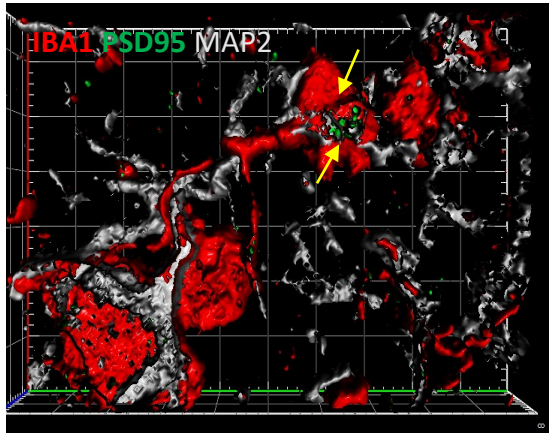
IBA1 PSD95 MAP2

c.

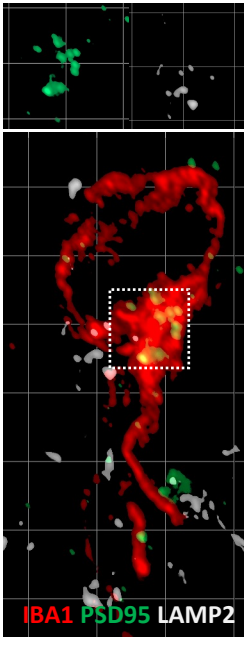
IBA1 PSD95 LAMP2

d.

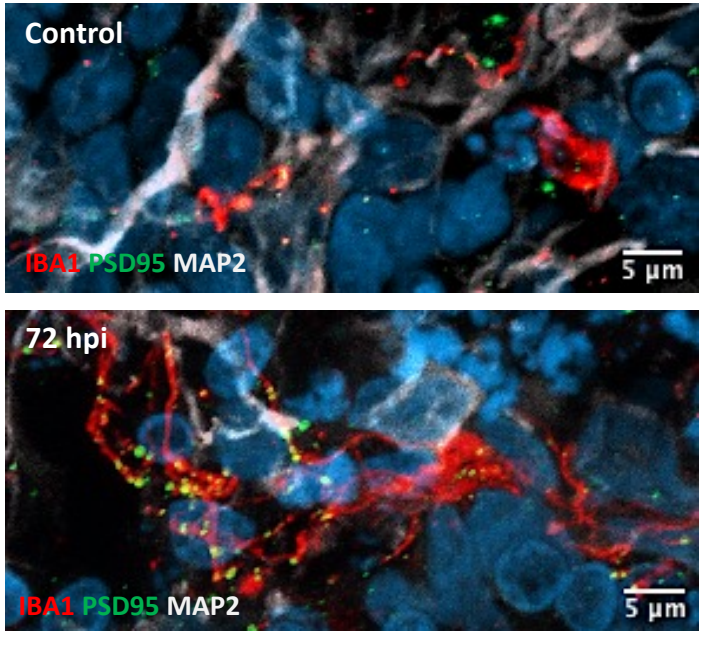
Control
IBA1 PSD95 MAP2
5 µm
72 hpi
IBA1 PSD95 MAP2
5 µm

e.

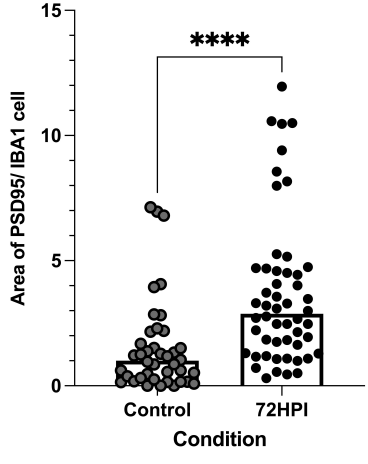
****
Area of PSD95/ IBA1 cell
15
10
5
0
Control
72HPI
Condition

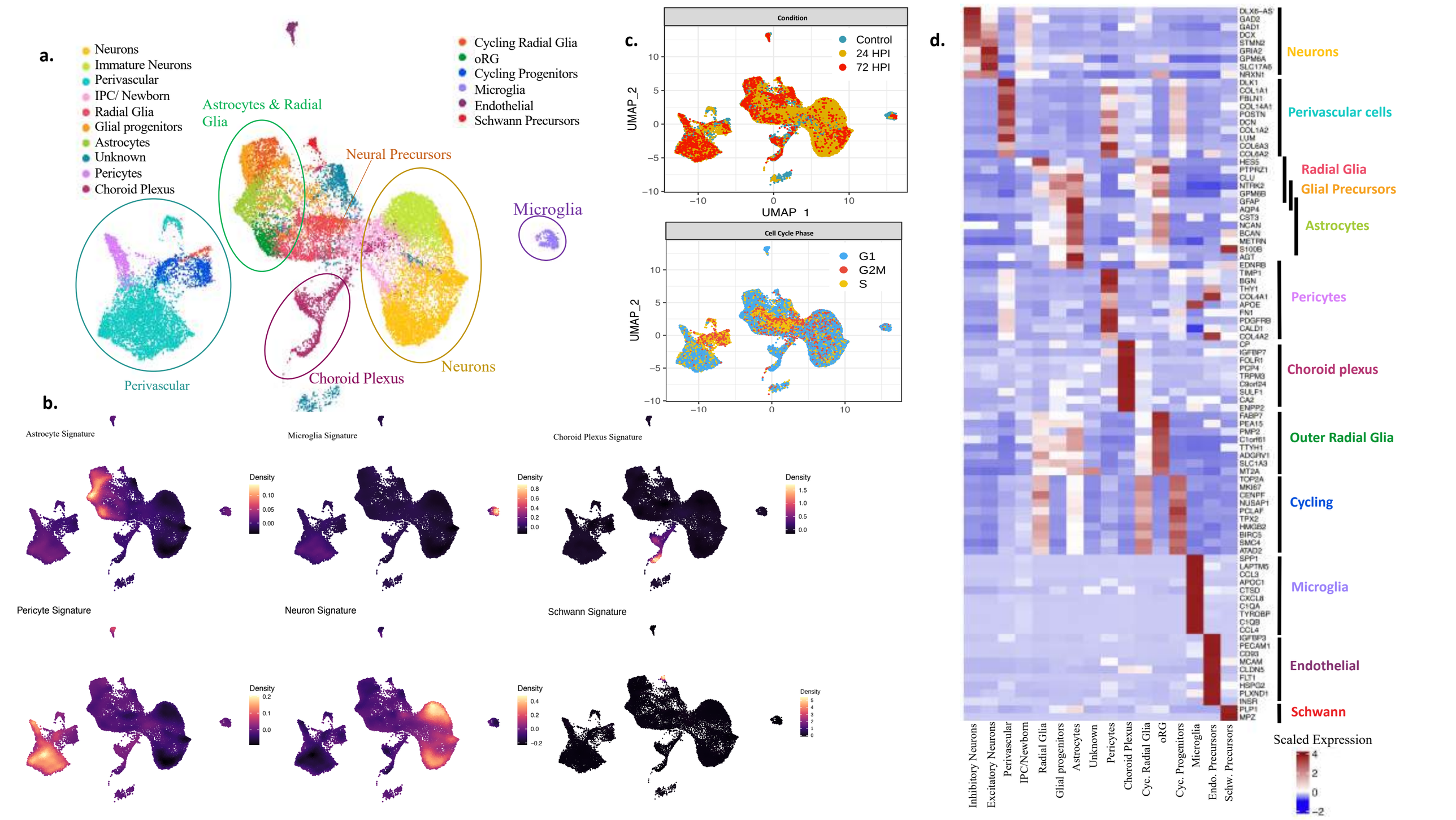
a.
Neurons
Immature Neurons
Perivascular
IPC/ Newborn
Radial Glia
Glial progenitors
Astrocytes
Unknown
Pericytes
Choroid Plexus
Cycling Radial Glia
oRG
Cycling Progenitors
Microglia
Endothelial
Schwann Precursors
Astrocytes & Radial Glia
Neural Precursors
Microglia
Perivascular
Choroid Plexus
Neurons
b.
Astrocyte Signature
Microglia Signature
Choroid Plexus Signature
Pericyte Signature
Neuron Signature
Schwann Signature
Density
c.
Condition
Control
24 HPI
72 HPI
UMAP_2
UMAP_1
Cell Cycle Phase
G1
G2M
S
d.
Neurons
Perivascular cells
Radial Glia
Glial Precursors
Astrocytes
Pericytes
Choroid plexus
Outer Radial Glia
Cycling
Microglia
Endothelial
Schwann
Inhibitory Neurons
Excitatory Neurons
Perivascular
IPC/Newborn
Radial Glia
Glial progenitors
Astrocytes
Unknown
Pericytes
Choroid Plexus
Cyc. Radial Glia
oRG
Cyc. Progenitors
Microglia
Endo. Precursors
Schw. Precursors
Scaled Expression

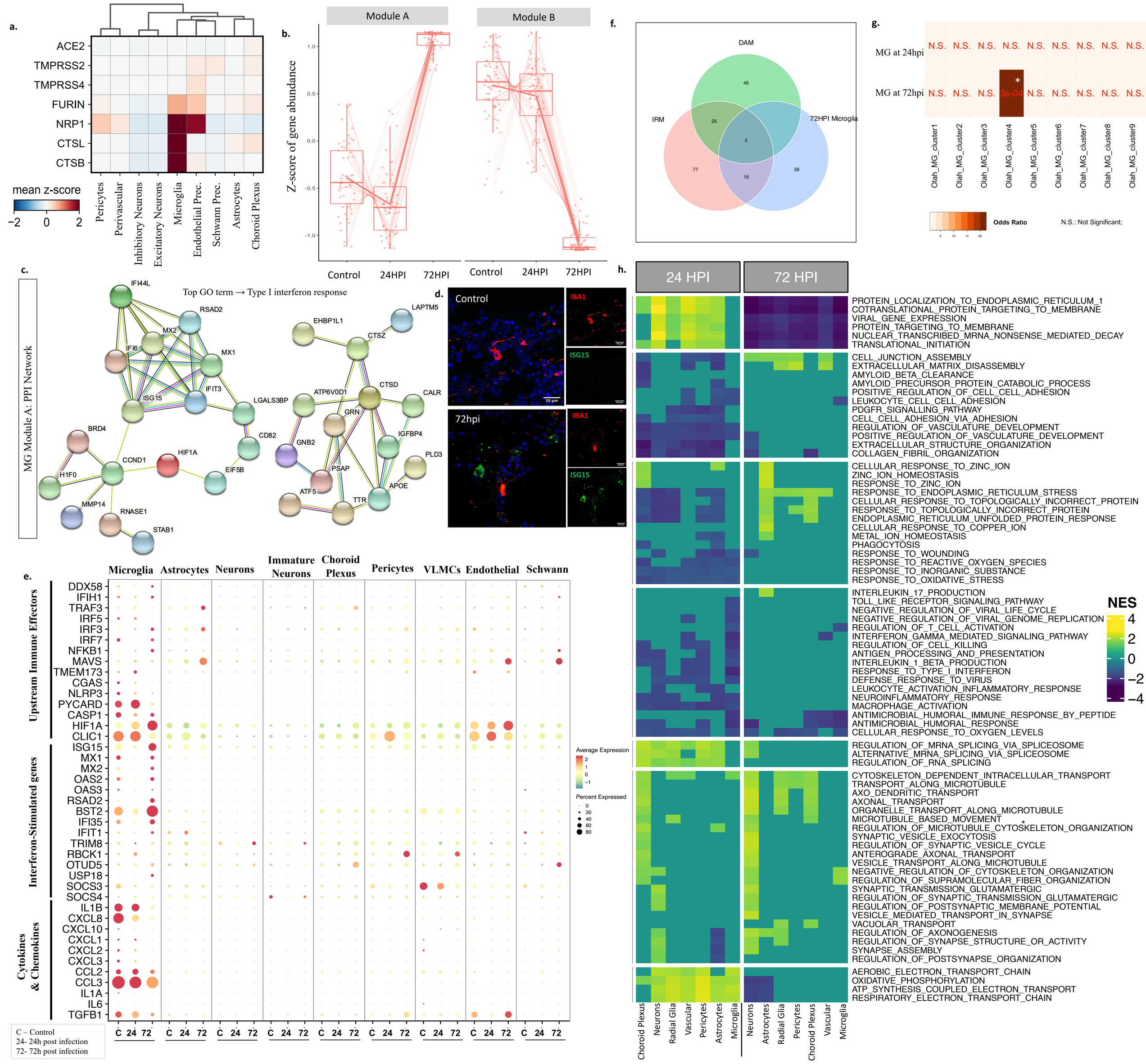
a.
ACE2
TMPRSS2
TMPRSS4
FURIN
NRP1
CTSL
CTSB
mean z-score
−2
0
2
Pericytes
Perivascular
Inhibitory Neurons
Excitatory Neurons
Microglia
Endothelial Prec.
Schwann Prec.
Astrocytes
Choroid Plexus
b.
Module A
Module B
Z-score of gene abundance
Control
24HPI
72HPI
f.
DAM
IRM
72HPI Microglia
49
25
2
77
19
39
g.
MG at 24hpi
MG at 72hpi
N.S.
3e-04
Olah_MG_cluster1
Olah_MG_cluster2
Olah_MG_cluster3
Olah_MG_cluster4
Olah_MG_cluster5
Olah_MG_cluster6
Olah_MG_cluster7
Olah_MG_cluster8
Olah_MG_cluster9
Odds Ratio
N.S.: Not Significant;
c.
MG Module A: PPI Network
Top GO term → Type I interferon response
IFI44L
RSAD2
MX2
IFI6
MX1
IFIT3
ISG15
LGALS3BP
BRD4
CD82
CCND1
HIF1A
H1F0
EIF5B
MMP14
RNASE1
STAB1
EHBP1L1
LAPTM5
CTSZ
ATP6V0D1
CTSD
CALR
GRN
GNB2
IGFBP4
PLD3
PSAP
ATF5
APOE
TTR
d.
Control
72hpi
IBA1
ISG15
20 µm
h.
24 HPI
72 HPI
PROTEIN_LOCALIZATION_TO_ENDOPLASMIC_RETICULUM_1
COTRANSLATIONAL_PROTEIN_TARGETING_TO_MEMBRANE
VIRAL_GENE_EXPRESSION
PROTEIN_TARGETING_TO_MEMBRANE
NUCLEAR_TRANSCRIBED_MRNA_NONSENSE_MEDIATED_DECAY
TRANSLATIONAL_INITIATION
CELL_JUNCTION_ASSEMBLY
EXTRACELLULAR_MATRIX_DISASSEMBLY
AMYLOID_BETA_CLEARANCE
AMYLOID_PRECURSOR_PROTEIN_CATABOLIC_PROCESS
POSITIVE_REGULATION_OF_CELL_CELL_ADHESION
LEUKOCYTE_CELL_CELL_ADHESION
PDGFR_SIGNALLING_PATHWAY
CELL_CELL_ADHESION_VIA_ADHESION
REGULATION_OF_VASCULATURE_DEVELOPMENT
POSITIVE_REGULATION_OF_VASCULATURE_DEVELOPMENT
EXTRACELLULAR_STRUCTURE_ORGANIZATION
COLLAGEN_FIBRIL_ORGANIZATION
CELLULAR_RESPONSE_TO_ZINC_ION
ZINC_ION_HOMEOSTASIS
RESPONSE_TO_ZINC_ION
RESPONSE_TO_ENDOPLASMIC_RETICULUM_STRESS
CELLULAR_RESPONSE_TO_TOPOLOGICALLY_INCORRECT_PROTEIN
RESPONSE_TO_TOPOLOGICALLY_INCORRECT_PROTEIN
ENDOPLASMIC_RETICULUM_UNFOLDED_PROTEIN_RESPONSE
CELLULAR_RESPONSE_TO_COPPER_ION
METAL_ION_HOMEOSTASIS
PHAGOCYTOSIS
RESPONSE_TO_WOUNDING
RESPONSE_TO_REACTIVE_OXYGEN_SPECIES
RESPONSE_TO_INORGANIC_SUBSTANCE
RESPONSE_TO_OXIDATIVE_STRESS
INTERLEUKIN_17_PRODUCTION
TOLL_LIKE_RECEPTOR_SIGNALING_PATHWAY
NEGATIVE_REGULATION_OF_VIRAL_LIFE_CYCLE
NEGATIVE_REGULATION_OF_VIRAL_GENOME_REPLICATION
REGULATION_OF_T_CELL_ACTIVATION
INTERFERON_GAMMA_MEDIATED_SIGNALING_PATHWAY
REGULATION_OF_CELL_KILLING
ANTIGEN_PROCESSING_AND_PRESENTATION
INTERLEUKIN_1_BETA_PRODUCTION
RESPONSE_TO_TYPE_I_INTERFERON
DEFENSE_RESPONSE_TO_VIRUS
LEUKOCYTE_ACTIVATION_INFLAMMATORY_RESPONSE
NEUROINFLAMMATORY_RESPONSE
MACROPHAGE_ACTIVATION
ANTIMICROBIAL_HUMORAL_IMMUNE_RESPONSE_BY_PEPTIDE
ANTIMICROBIAL_HUMORAL_RESPONSE
CELLULAR_RESPONSE_TO_OXYGEN_LEVELS
REGULATION_OF_MRNA_SPLICING_VIA_SPLICEOSOME
ALTERNATIVE_MRNA_SPLICING_VIA_SPLICEOSOME
REGULATION_OF_RNA_SPLICING
CYTOSKELETON_DEPENDENT_INTRACELLULAR_TRANSPORT
TRANSPORT_ALONG_MICROTUBULE
AXO_DENDRITIC_TRANSPORT
AXONAL_TRANSPORT
ORGANELLE_TRANSPORT_ALONG_MICROTUBULE
MICROTUBULE_BASED_MOVEMENT
REGULATION_OF_MICROTUBULE_CYTOSKELETON_ORGANIZATION
SYNAPTIC_VESICLE_EXOCYTOSIS
REGULATION_OF_SYNAPTIC_VESICLE_CYCLE
ANTEROGRADE_AXONAL_TRANSPORT
VESICLE_TRANSPORT_ALONG_MICROTUBULE
NEGATIVE_REGULATION_OF_CYTOSKELETON_ORGANIZATION
REGULATION_OF_SUPRAMOLECULAR_FIBER_ORGANIZATION
SYNAPTIC_TRANSMISSION_GLUTAMATERGIC
REGULATION_OF_SYNAPTIC_TRANSMISSION_GLUTAMATERGIC
REGULATION_OF_POSTSYNAPTIC_MEMBRANE_POTENTIAL
VESICLE_MEDIATED_TRANSPORT_IN_SYNAPSE
VACUOLAR_TRANSPORT
REGULATION_OF_AXONOGENESIS
REGULATION_OF_SYNAPSE_STRUCTURE_OR_ACTIVITY
SYNAPSE_ASSEMBLY
REGULATION_OF_POSTSYNAPSE_ORGANIZATION
AEROBIC_ELECTRON_TRANSPORT_CHAIN
OXIDATIVE_PHOSPHORYLATION
ATP_SYNTHESIS_COUPLED_ELECTRON_TRANSPORT
RESPIRATORY_ELECTRON_TRANSPORT_CHAIN
NES
4
2
0
−2
−4
Choroid Plexus
Neurons
Radial Glia
Vascular
Pericytes
Astrocytes
Microglia
e.
Microglia
Astrocytes
Neurons
Immature Neurons
Choroid Plexus
Pericytes
VLMCs
Endothelial
Schwann
Upstream Immune Effectors
Interferon-Stimulated genes
Cytokines & Chemokines
DDX58
IFIH1
TRAF3
IRF5
IRF3
IRF7
NFKB1
MAVS
TMEM173
CGAS
NLRP3
PYCARD
CASP1
HIF1A
CLIC1
ISG15
MX1
MX2
OAS2
OAS3
RSAD2
BST2
IFI35
IFIT1
TRIM8
RBCK1
OTUD5
USP18
SOCS3
SOCS4
IL1B
CXCL8
CXCL10
CXCL1
CXCL2
CXCL3
CCL2
CCL3
IL1A
IL6
TGFB1
Average Expression
Percent Expressed
C 24 72
C – Control
24- 24h post infection
72- 72h post infection

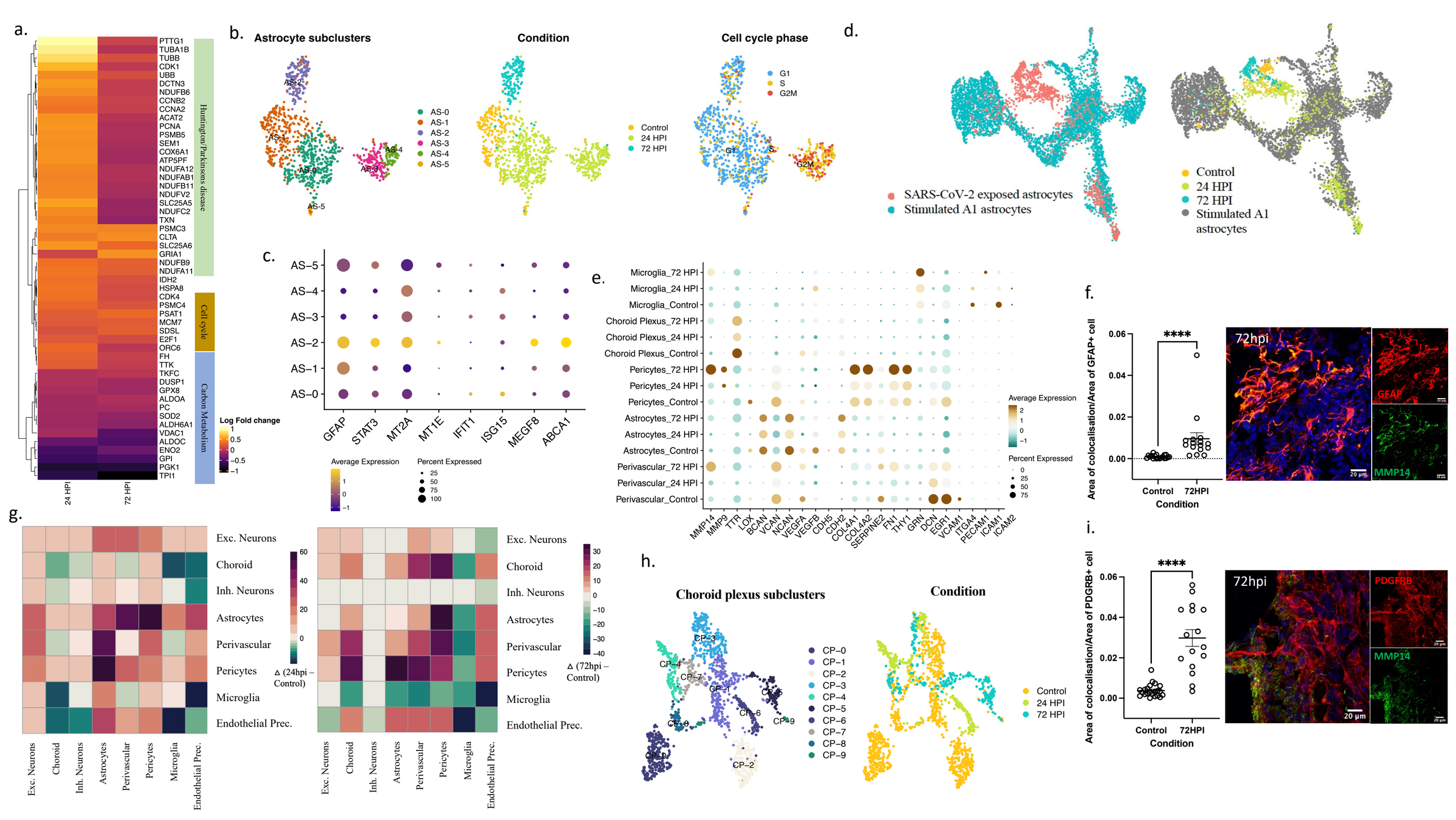
a.
PTTG1
TUBA1B
TUBB
CDK1
UBB
DCTN3
NDUFB6
CCNB2
CCNA2
ACAT2
PCNA
PSMB5
SEM1
COX6A1
ATP5PF
NDUFA12
NDUFAB1
NDUFB11
NDUFV2
SLC25A5
NDUFC2
TXN
PSMC3
CLTA
SLC25A6
GRIA1
NDUFB9
NDUFA11
IDH2
HSPA8
CDK4
PSMC4
PSAT1
MCM7
SDSL
E2F1
ORC6
FH
TTK
TKFC
DUSP1
GPX8
ALDOA
PC
SOD2
ALDH6A1
VDAC1
ALDOC
ENO2
GPI
PGK1
TPI1
Huntington/Parkinsons disease
Cell cycle
Carbon Metabolism
Log Fold change
24 HPI
72 HPI
b.
Astrocyte subclusters
Condition
Cell cycle phase
AS-0
AS-1
AS-2
AS-3
AS-4
AS-5
Control
24 HPI
72 HPI
G1
S
G2M
c.
AS–5
AS–4
AS–3
AS–2
AS–1
AS–0
GFAP
STAT3
MT2A
MT1E
IFIT1
ISG15
MEGF8
ABCA1
Average Expression
Percent Expressed
d.
SARS-CoV-2 exposed astrocytes
Stimulated A1 astrocytes
Control
24 HPI
72 HPI
Stimulated A1 astrocytes
e.
Microglia_72 HPI
Microglia_24 HPI
Microglia_Control
Choroid Plexus_72 HPI
Choroid Plexus_24 HPI
Choroid Plexus_Control
Pericytes_72 HPI
Pericytes_24 HPI
Pericytes_Control
Astrocytes_72 HPI
Astrocytes_24 HPI
Astrocytes_Control
Perivascular_72 HPI
Perivascular_24 HPI
Perivascular_Control
MMP14
MMP9
TTR
LOX
BCAN
VCAN
NCAN
VEGFA
VEGFB
CDH5
CDH2
COL4A1
COL4A2
SERPINE2
FN1
THY1
GRN
DCN
EGR1
VCAM1
ITGA4
PECAM1
ICAM1
ICAM2
Average Expression
Percent Expressed
f.
Area of colocalisation/Area of GFAP+ cell
****
Control
72HPI
Condition
72hpi
GFAP
MMP14
20 µm
g.
Exc. Neurons
Choroid
Inh. Neurons
Astrocytes
Perivascular
Pericytes
Microglia
Endothelial Prec.
Δ (24hpi – Control)
Δ (72hpi – Control)
h.
Choroid plexus subclusters
Condition
CP–0
CP–1
CP–2
CP–3
CP–4
CP–5
CP–6
CP–7
CP–8
CP–9
Control
24 HPI
72 HPI
i.
Area of colocalisation/Area of PDGRB+ cell
****
Control
72HPI
Condition
72hpi
PDGFRB
MMP14
20 µm